Development and Evaluation of Data Processing Techniques in Magnetoencephalography

Development and Evaluation of Data Processing Techniques in Magnetoencephalography

Von der Fakultät für Mathematik und Informatik
der Universität Leipzig
angenommene

DISSERTATION

zur Erlangung des akademischen Grades

DOCTOR RERUM NATURALIUM
(Dr. rer. nat.)

im Fachgebiet

INFORMATIK

vorgelegt von Dipl.-Phys. Margit Schönherr
geboren am 13. August 1983 in Leipzig

Die Annahme der Dissertation haben empfohlen:

Prof. Dr. Gerik Scheuermann
Bild- und Signalverarbeitung, Universität Leipzig
Prof. Dr.-Ing. habil. Jens Haueisen
Institut für Biomedizinische Technik und Informatik, TU Ilmenau

Tag der Verleihung: 12. Juli 2012

Bibliographical data

Schönherr, Margit

Development and Evaluation of Data Processing Techniques in Magnetoencephalography

University of Leipzig, dissertation, 117 pages, 58 references, 57 figures, 2 tables

Abstract

A recurrent issue in MEG data analysis is the identification and elimination of unwanted interference within the recorded signal. Various strategies exist to meet this purpose. In this thesis, two of these strategies are scrutinized in detail. The first is the commonly used procedure of averaging over trials. Although being a successfully applied data reduction method, averaging can eliminate valuable information and is only appropriate under certain conditions. Alternative approaches aiming at single trial analysis, however, are currently not readily available. In the first part of this dissertation, a compromise involving random subaveraging of trials is presented. The principles of the new method are described and numerous examples demonstrate its applicability in the context of source localization. As a result, inferences about the generators of single trials can be drawn which allows deeper insight into neuronal processes of the human brain.

The second technique examined in this thesis is a preprocessing tool termed Signal Space Separation (SSS). The mathematical principles and the rules for its application are investigated. It turns out that the SSS method works reliably, even when the mathematical preconditions are not fully obeyed. Furthermore, the utilization of the SSS method for the transformation of MEG data onto the scalp surface is studied. The results are discussed in comparison to those produced by inverse and subsequent forward computation. It ensues that the latter approach yields superior results for the intended purpose of data transformation.

Contents

Symbols and Abbreviations

Symbols

$\mathbf{B}$	magnetic flux density (induction)
$\mathbf{D}$	electric flux density (dielectric displacement current)
d_{orig}	distance of sources to coordinate origin
d_{sen}	distance of sources to closest sensor
$\mathbf{E}$	electric field
$\mathbf{H}$	magnetic field
I	electric current
$\mathbf{J}$	electric current dipole
$\mathbf{L}$	leadfield
M	number of sensors
N	number of sources
$\mathbf{r}$	sensor location
$\mathbf{r}'$	source location
V	scalar potential

ϵ	electric permeability
μ	magnetic permeability
ρ	charge density
σ	electric conductivity
ϕ	measurement vector
$\hat{\phi}$	estimated measurement vector

Abbreviations

BEM	boundary element method
BOLD	blood oxygenation level dependent
CSF	cerebrospinal fluid
CT	(X-ray) computer tomography
DC	direct current
ECD	equivalent current dipole
EEG	electroencephalography
ERF	event related field
FEM	finite element method
fMRI	functional magnetic resonance imaging
ISI	inter-stimulus interval
MCG	magnetocardiography
MEG	magnetoecephalography
MMN	mismatch negativity
MRS	magnetic resonance spectroscopy
PET	positron emission tomography
PSP	post-synaptic potential
ROI	region of interest
SNR	signal-to-noise ratio
SPECT	single photon emission computer tomography
SQUID	superconducting quantum interference device
SSS	Signal Space Separation
VSH	vector spherical harmonics

Chapter 1

Introduction

1.1 Survey of brain imaging techniques

During the past decades, a number of brain imaging techniques has been developed which enable the visualization of anatomical and functional structures in the human brain. Quickly, they found their way into medicine as well as cognitive neuroscience. Medical applications range over tumor diagnostics and epilepsy surgery, for example. Especially functional brain imaging advanced basic research on neuropsychological topics and addressed questions related to physiological and pathological brain processes.

This introduction will give a brief overview of different brain imaging techniques in a non-exhaustive way. Summarizing the explanations presented by Jänke (2005), the working principles of the methods are outlined shortly and advantages and drawbacks are contrasted.

As the first anatomical tool, X-ray Computed Tomography (CT) was introduced in 1971. It was used to obtain three dimensional images by passing highly focused X-ray beams through the brain and recording their attenuation (Raichle, 2008).

Another means for studying brain anatomy is Magnetic Resonance Imaging (MRI). The technique also known as Nuclear Magnetic Resonance (NMR) had been applied mainly for research in chemistry so far. It relies on the physical properties of protons. Their spins align in parallel when

exposed to a strong external magnetic field. Radio frequency pulses bring the protons from equilibrium into an excited state. When they return to the ground state, radiation is emitted whose intensity varies for different tissue types. Due to its sensitivity to soft tissue, MRI produces much more detailed images than CT.

The first methods to image brain functioning were Positron Emission Tomography (PET) and Single Photon Emission Computer Tomography (SPECT). Here, some radioactive molecules are administered which are known to increase their concentration in metabolic active areas. The detection of emitted gamma-radiation (i.e. photons) gives information about metabolism processes, whereas morphology is represented only vaguely. The major drawback of these techniques is that they are invasive, since radioactive substances must be applied.

With functional MRI (fMRI) blood oxygenation level dependent (BOLD) changes in metabolism can be made visible. In metabolically active brain areas, the oxygen supply is increased. The BOLD contrast arises from the fact that deoxygenated hemoglobin behaves like a little magnet. Owing to the presence of iron, it is detectable by MRI. In oxygenated hemoglobin, however, the iron is 'neutralized', so it does not interact with the magnetic field (Raichle, 2008). Compared to PET or SPECT, high spatial resolution can be achieved with fMRI. However, all of these methods are based on indirect measures of neuronal activity, implicating a temporal delay to the observed parameters.

Studying brain processes more directly is possible with Electro- and Magnetoencephalography (EEG/MEG). With these completely non-invasive techniques, electric potentials or magnetic fields are measured, respectively. They are generated by tiny currents in activated neurons and make neuronal processes visible with millisecond time resolution. Due to methodological issues which will be discussed in chapter 2, the spatial resolution is usually lower than that of PET and fMRI (Baillet et al., 2001).

Figure 1.1[1] summarizes the properties of the functional brain imaging techniques described. It relates spatial and temporal resolution and indicates invasiveness by color coding.

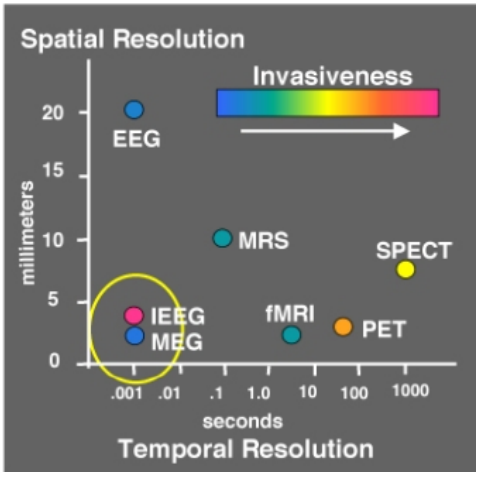

Figure 1.1: Properties of functional brain imaging techniques described in the text. Two additional methods are shown: Magnetic Resonance Spectroscopy (MRS) and invasive EEG (iEEG).

1.2 The scope of this thesis

One of the most powerful applications of MEG is the localization of brain activity. Therefore, the neural mechanisms have to be understood and electromagnetic processes have to be expressed mathematically. In chapter 2, the biological basics of neuronal currents and the generation of the magnetic signal are shortly described. An introduction to the technical setup and operation of an MEG device is given. Furthermore, the physical and mathematical background for modeling electric and magnetic properties of biological tissue is presented. Finally, the basic principles for the solution of the forward and inverse electromagnetic problem are elucidated.

Since source reconstruction highly depends on the quality of the recorded signals, the noise level is an important characteristic to describe the data.

[1]Modified from http://web.mit.edu/kitmitmeg/MEG_Work_5.jpg (17.12.2011)

If the signal-to-noise ratio (SNR) is too low, source localization becomes impossible, and also moderate interference can impair correct source estimation considerably. So the major concern of this thesis is the development and evaluation of MEG data analysis methods for the separation of signal and interference. On top of conventional filtering and averaging, different strategies to refine and analyze the data will be developed and appraised.

Chapter 3 deals with the problems of averaging. All measured MEG data consist of a combination of brain activity and external interference. Elaborate filtering of raw MEG data as a first processing step usually serves different purposes. Slow baseline drifts are removed and the frequency range is confined to the interesting neuronal frequencies below 100 Hz (Smith et al., 1990). In many cases only frequencies of about 1-30 Hz are considered, which suppresses a lot of environmental interference at an early stage of data analysis, for example 50 Hz power-line interference.

However, there is not only environmental noise in the data, but also spontaneous brain activity which is not time-locked to any external stimulation. Averaging is a strong data reduction method and an efficient way to eliminate this ongoing activity in favor of evoked brain activity. Nevertheless, there might be a great deal of information in the data that is not phase-locked and gets lost during the averaging process. Moreover, the brain's responses to repeated stimuli are not identical. Induced responses do not solely depend on the characteristics of the stimulus, but also on the subject's performance and psychophysiological state. The brain is always active and a stimulus can be regarded as a perturbation of ongoing activity. So Laskaris and Ioannides (2002) point out that any possible interactions between successive single trial responses, or between spontaneous and evoked brain activity might be overlooked by averaging.

These considerations led to the development of a method to analyze the data characteristics of single trials, which is described in chapter 3. With the help of numerous simulations the range of miscellaneous applications of the novel procedure is demonstrated.

In chapter 4, the recently developed Signal Space Separation (SSS) method will be investigated in detail (Taulu and Kajola, 2005). SSS is a widely used preprocessing tool for MEG data having numerous applications, for example noise cancellation and head movement compensation (Taulu et al., 2005). It is essentially based on a series expansion of the measured magnetic field, which distinguishes uniquely between fields originating from neuronal sources and fields produced by external interference. The mathematical conditions for convergence of the series expansion, as well as the consequences of violations of these conditions will be scrutinized in this chapter.

In chapter 5, the SSS method will be employed for a more extended version of data transformation. Going beyond head movement correction and data transformation between different MEG devices, individual virtual sensor arrays will be defined. The aim is to transform MEG data directly onto the head surface for better comparability with EEG data, for example. The principle of the approach and its limitations will be studied by simulations.

Chapter 2

Theoretical fundamentals of MEG

2.1 The physiological basis of MEG

This section is meant to give a short introduction into the neurophysiological mechanisms that give rise to electromagnetic signals outside the head. It is merely an overview, a more detailed description is provided by Hülshoff (2000) or Malmivuo and Plonsey (1995).

Each neuronal cell consists of many dendrites, the cell body, and an axon and is connected to other neurons by synapses. Information is received by the dendrites and relayed via the axon. Within a neuron, signals are carried electrically, whereas information transfer between different neurons, muscles, or sensory receptors takes place chemically. Inside a neuron at rest there is a surplus of potassium ions (K^+) and a lack of sodium ions (Na^+). Additionally, the cell has a resting potential of -70 mV compared to the extracellular space. A schematic pyramidal cell of the human cortex is displayed in figure 2.1.

When a signal from an axon reaches a synapse, this leads to an output of some chemical into the synaptic cleft. This opens ion channels at the adjacent neuronal cell and the ion flow builds up a post-synaptic potential (PSP) across its membrane. The PSP can increase the potential difference

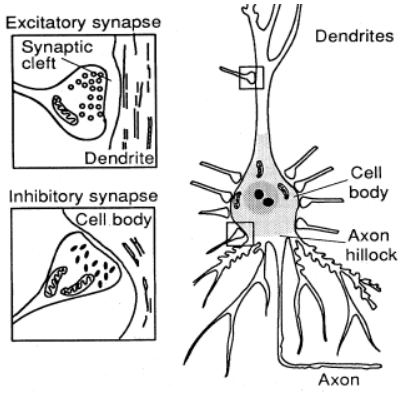

Figure 2.1: Schematic pyramidal neuronal cell, modified from (Hämäläinen et al., 1993).

between intracellular and extracellular space (inhibitory, hyperpolarizing), or decrease the potential difference (excitatory, depolarizing). If an excitatory PSP exceeds a certain threshold at the axon hillock, an action potential is created in this cell and will be transported further through its axon to other cells.

The action potential of about +30 mV activates the neuronal cell and opens channels in the membrane to enable sodium ions to get in. A depolarization wave front travels along the axon. Compensation of electrical charges is achieved through potassium ions flowing out, leading to repolarization. Due to the disturbed K^+ - Na^+ equilibrium, now potassium ions have to be pumped into and sodium ions out of the cell. This process of restoring the original ion distribution consumes energy and takes some time. During this absolute refractory period no further signals can be passed.

Both the action potential and the PSP cause intracellular current flow, the so-called primary currents, and due to conservation of electrical charges also extracellular secondary or volume currents can be observed. A large number of simultaneous potentials (10.000-100.000) is needed to create an extracranially detectable signal, because the single contributions are so small.

The action potentials are relatively short in time (about 1 ms), the depolarization and repolarization waves are traveling, and they produce two opposite currents which can be seen as a quadrupolar current from a distance. For these reasons, the action potentials in different cells are rather unlikely to occur synchronously. So the extracranial fields are mainly generated by the excitatory PSPs which are spatially less distributed and present for about 10 ms. Thus, the apical dendrites of the cortical pyramidal cells which are aligned in parallel are considered to be the principal generators of MEG and EEG signals.

The center of these neuronal sources is modeled by an equivalent current dipole (ECD), since the measured field patterns are similar to the field of a current dipole, and it is a good approximation for a small source viewed from a remote position (Sarvas, 1987). The currents flow perpendicular to the cortical surface, so because of the convoluted structure of the cortex, the orientations of the currents change. This is illustrated in figure 2.2.

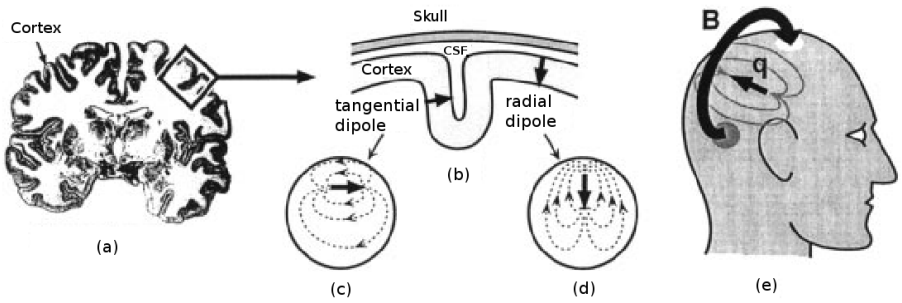

Figure 2.2: (a) Coronal section of the human brain. (b) Different dipole orientations because of convoluted cortex. (c) Tangential source produces external magnetic field. (d) Radial source does not produce external magnetic field. (e) Magnetic field of a tangential current dipole. Modified from (Vrba and Robinson, 2001).

MEG can only detect magnetic fields of dipoles lying tangentially to the skull surface because these fields leave and re-enter the head whereas the fields of radial sources do not. They are thus called magnetically silent

sources. In fact, radial sources exist in exact spherical symmetry only, but also in realistically shaped head models they produce signals five to ten times smaller than tangential sources.

2.2 Recording of MEG

The measurement of biomagnetic signals is a challenging task, since the magnetic fields due to neuronal activity are much smaller than the fields of the surrounding environment. Figure 2.3[2] illustrates the different orders of magnitude. Obviously, neuronal magnetic fields typically range between fT and a few pT, which is one billion or one million times weaker than the earth's magnetic field of 50 μT, and still at least three orders of magnitude smaller than the fields from external noise sources.

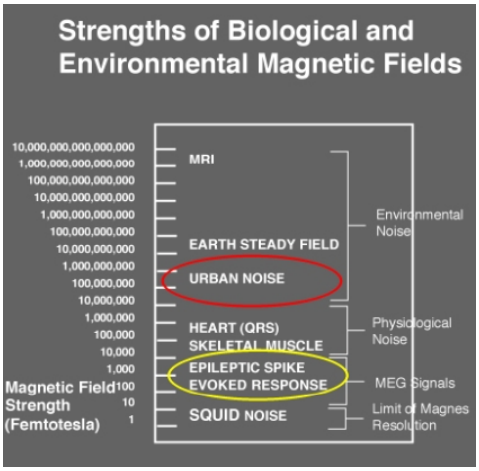

Figure 2.3: Comparison of magnetic field strengths produced by different sources. Neuronal sources are marked with yellow, environmental noise is indicated with red. Biological noise is settled in between.

Hence extremely sensitive detectors and elaborate noise reduction methods are required. Here, only a brief overview of the operation principles of MEG is given. More detailed insight is provided for example by Hämäläinen et al. (1993) and Vrba and Robinson (2001).

[2]Modified from http://web.mit.edu/kitmitmeg/MEG_Work_5.jpg (17.12.2011)

Currently, for measuring the tiny neuromagnetic signals, superconducting quantum interference devices (SQUIDs) are used almost exclusively. The SQUIDs are coupled to small conductor loops, the so-called flux transformers which consist of a pick-up coil and a coupling coil. The field change perpendicular to the face of the pick-up coil induces a voltage. Since the whole flux transformer is superconducting, this voltage causes a loss-free current which produces a magnetic field within the coupling coil. This magnetic field is detected by the SQUIDs.

The employed dc SQUIDs (direct current SQUIDs) consist of a superconducting ring with two insulating layers, the Josephson junctions. Electrons tunneling through the Josephson junctions show quantum interference dependent on the strength of the magnetic field. Little changes in the magnetic field make the junctions behave like a resistor and so enable the measurement of such tiny changes as produced by neuronal currents.

Both the SQUIDs and the flux transformers are superconducting and have to be operated at very low temperature. They are assembled in an insulating dewar which is cooled with liquid helium (4.2 K). Usually, the entire MEG system is surrounded by a magnetically shielding chamber to minimize environmental interference.

Today's whole head MEG systems can comprise various pick-up coil arrangements leading to different sensor types. The most common ones

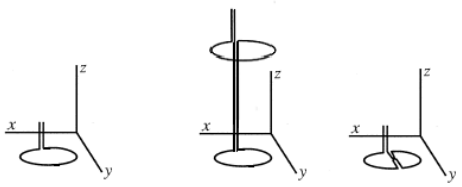

Figure 2.4: Left: Magnetometer with a single pick-up coil measuring B_z. Middle: First order axial gradiometer with two antiparallel pick-up coils measuring $\partial B_z/\partial z$. Right: Planar gradiometer with two antiparallel pick-up coils measuring $\partial B_z/\partial x$. Modified from (Hämäläinen et al., 1993).

are displayed in figure 2.4. A magnetometer consists of a single wire loop and is the most basic sensor. The combination of two or more loops with antiparallel orientation is called gradiometer. In axial gradiometers the coils are placed above each other, in planar gradiometers they are in the same plane.

Gradiometers measure changes of the magnetic field along their latitude. As the magnetic field of a dipole in distance r decreases with r^{-2}, the gradient of this field decreases with r^{-3}. So depending on their baseline (the distance between the two pick-up coils) gradiometers behave like spatial highpass filters and damp signals from distant sources.

The MEG data used in the present thesis have been acquired by the 306 channel VectorView device of Elekta Neuromag Oy (Helsinki, Finland), comprising 102 magnetometers and 204 planar gradiometers. It is shown in figure 2.5 (a)[3]. Figure 2.5 (b)[4] depicts the 102 sensor chips, each containing one magnetometer and two orthogonal gradiometers.

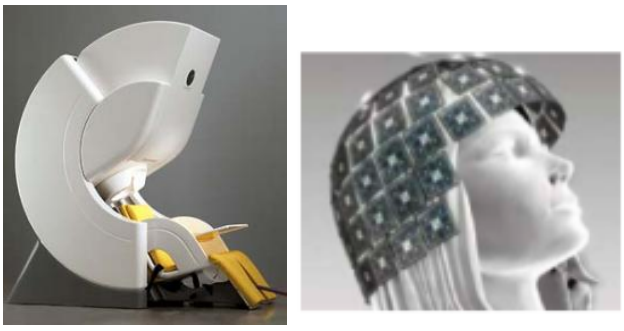

(a) (b)

Figure 2.5: (a) Elekta Neuromag MEG system, (b) Arrangement of the sensor chips.

[3]Taken from http://www.itnonline.com/sites/default/files/imagecache/node_image/photo_article/meg_side.jpg (17.12.2011)

[4]Taken from http://www.orasimedical.com/_visuals/gray_meg_cap.png (17.12.2011)

2.3 Forward modeling

2.3.1 Electromagnetic laws

This section describes how an electrical current produces a magnetic field. An extensive presentation of this can be found in the literature about the basic concepts of electrodynamics, for example (Greiner, 1982). A short and demonstrative introduction is given by Pfeifer and Schmiedel (1997).

The laws of electrodynamics are summarized by Maxwell's equations. They combine the findings of many scientists who studied the properties of electrical charges and currents and the magnetic fields induced by these currents.

$$\begin{aligned} \nabla \mathbf{D} &= \rho \\ \nabla \mathbf{B} &= 0 \\ \nabla \times \mathbf{E} &= -\dot{\mathbf{B}} \\ \nabla \times \mathbf{H} &= \mathbf{J} + \dot{\mathbf{D}} \end{aligned}$$

Here, $\mathbf{D}$ denotes the dielectric displacement current, $\mathbf{B}$ the magnetic flux density, $\mathbf{E}$ the electric field, and $\mathbf{H}$ the magnetic field. ρ is the charge density, $\mathbf{J}$ is the current density, and the dot indicates time derivatives.

The relations between the fields and the flux densities are given by

$$\begin{aligned} \mathbf{D} &= \epsilon_r \epsilon_0 \mathbf{E} \\ \mathbf{B} &= \mu_r \mu_0 \mathbf{H}, \end{aligned}$$

where ϵ_x and μ_x are electric and magnetic permeabilities of matter ($x = r$) and vacuum ($x = 0$). For biological tissue the magnetic susceptibility $\chi = \mu_r - 1 \approx 10^{-6}$, thus the relative permeability $\mu_r \approx 1$ and it is constant over the whole volume (Wolters et al., 2004). Hence, the tissue is diamagnetic and transparent for magnetic fields (Smith et al., 1990).

Furthermore, in the case of neuronal currents, the considered frequencies are below 2000 Hz. This means that the capacitive effect of tissue

conductivity, the inductive effect, and the electromagnetic propagation effect are negligible (Wolters et al., 2004). It is appropriate to set all time-derivatives to zero, resulting in the quasi-static approximation of Maxwell's equations. Only tissue resistivity is essential (Malmivuo and Plonsey, 1995):

$$\begin{aligned} \nabla \times \mathbf{E} &= 0 \qquad \Rightarrow \qquad \mathbf{E} = -\nabla V \\ \nabla \times \mathbf{H} &= \mathbf{J} \qquad \Rightarrow \qquad \nabla \times \mathbf{B} = \mu_0 \mathbf{J}, \end{aligned} \tag{2.1}$$

where V is the electric potential.

Using Biot-Savart's law (eq. (2.2)), the magnetic field of an arbitrary stationary current density $\mathbf{J}$ at source location $\mathbf{r}'$ can be computed. It has been found out empirically from many detailed experiments and solves Maxwell's equation (2.1).

$$\mathbf{B}(\mathbf{r}) = \frac{\mu_0}{4\pi} \int_\Omega \frac{\mathbf{J}(\mathbf{r}') \times (\mathbf{r} - \mathbf{r}')}{|\mathbf{r} - \mathbf{r}'|^3} \mathrm{d}^3\mathbf{r}' \tag{2.2}$$

The integration volume Ω extends over the source space containing $\mathbf{J}$. The current density $\mathbf{J}$ consists of the primary current $\mathbf{J}_p$, which reflects neuronal activity, and the ohmic volume currents, which depend on the conductivity σ.

$$\mathbf{J} = \mathbf{J}_p + \sigma \mathbf{E}$$

It has been shown that in an infinite homogeneous medium the total current density can be replaced by the primary current density $\mathbf{J}_p$, and that $\sigma\mathbf{E}$ does not contribute to the magnetic field (Sarvas, 1987).

2.3.2 Volume conduction

The Biot-Savart law cannot be applied to MEG or EEG forward modeling, though, because the conductivities within the head are inhomogeneous. σ is not a constant value, but rather a tensor that depends on tissue type and orientation. Thus, the magnetic field as well as the electric potential are distorted by volume conduction and spread anisotropically. In order to describe the field propagation through the head mathematically, a model

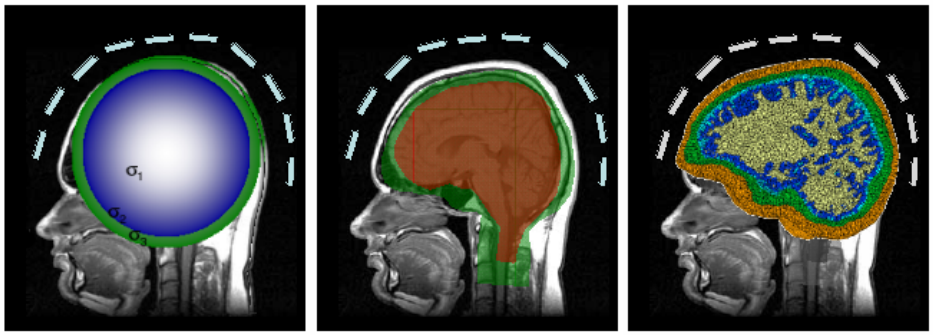

Figure 2.6: Volume conductor models: Sphere model (left), BEM model (middle), FEM model (right, modified from (Wolters, 2003)).

of the head as a volume conductor is necessary. The three most commonly used models are shown in figure 2.6.

For the spherical volume conductor model, concentric spheres are fitted to the head shape and different conductivities are assumed for brain, skull, and skin. For MEG, mostly a single sphere with a constant brain conductivity is sufficient, because the magnetic field outside the conducting volume is independent of the conductivity profile $\sigma = \sigma(r)$ (Sarvas, 1987).

The boundary element method (BEM) and the finite element method (FEM) are common techniques to solve the electromagnetic forward problem with realistically shaped head models. Therefore, the various tissues are segmented based on anatomical MR images.

In the BEM approach, the interfaces between regions of different conductivities are represented by meshes. On the nodes, the fields are calculated in terms of basic solutions and form secondary sources. For MEG and also for most applications of EEG, BEM models have turned out to be sufficiently accurate (Gencer et al., 1998). Again, for MEG usually one layer is enough, whereas for EEG at least three BEM layers are needed because of the highly different conductivity values of brain, skull, and skin. As a consequence, forward modeling is computationally less expensive and source localization usually more accurate with MEG than with EEG.

For FEM modeling, the volume of interest is divided into volume ele-

ments, and for each element a linear equation system is derived to calculate local node potentials. The distinct conductivities of skin, skull, cerebrospinal fluid (CSF), gray matter, and white matter can be taken into account. In addition, it facilitates modeling of conductivity inhomogeneity and anisotropy. So FEM modeling is particularly important in the presence of tumors or holes in the skull after brain surgery.

Although it was a time-consuming procedure in the past, new algorithms have been developed recently, which are able to speed up the computations by a factor of more than 100 (Wolters et al., 2004). Furthermore, with N being the number of nodes in the mesh, the computational complexity of FEM scales linearly ($O(N)$), whereas the cost of computing the BEM coefficient matrix is quadratic ($O(N^2)$) (Gencer et al., 1998). This makes FEM more appropriate when realistic volume conductor models with high resolution are needed.

2.3.3 MEG forward equation

When taking into account volume conduction effects, in general, the resulting differential equations do not have an analytical solution, and they have to be solved numerically by iteration. Only for the highly simplified case of spherical symmetry, an analytical formula of the magnetic field can be given. An extended derivation is provided in (Sarvas, 1987), here only the results will be summarized.

Assuming a single primary current dipole $\mathbf{J}_p$ at $\mathbf{r}'$ with dipole moment $\mathbf{Q}$, it can be written with Dirac's delta distribution as $\mathbf{J}_p = \delta(\mathbf{r} - \mathbf{r}')\mathbf{Q}$. Using this, Biot-Savart's law in equation (2.2) reduces to

$$\mathbf{B}(\mathbf{r}) \;=\; \frac{\mu_0}{4\pi}\mathbf{Q} \times \frac{\mathbf{r} - \mathbf{r}'}{|\mathbf{r} - \mathbf{r}'|^3}.$$

Incorporating volume conduction, the magnetic field outside a spheri-

cally symmetric volume conductor is given by equation (2.3)

$$\begin{aligned} \mathbf{a} &= \mathbf{r} - \mathbf{r}' \\ F &= a^2 r\Big(1 + \frac{\mathbf{a}\cdot\mathbf{r}}{a\cdot r}\Big) \\ \mathbf{B}(\mathbf{r}) &= \frac{\mu_0}{4\pi F^2}(F\mathbf{Q}\times\mathbf{r}' \;-\; \mathbf{Q}\times\mathbf{r}'\cdot\mathbf{r}\cdot\nabla F), \end{aligned} \tag{2.3}$$

where $a = |\mathbf{a}|$, $r = |\mathbf{r}|$, and the gradient of F is computed by the following equation, (Grunwald, 1996).

$$\begin{aligned} \alpha &= \frac{a^2}{r} + 2a + 2r + \frac{\mathbf{ar}}{a} \\ \beta &= a + 2r + \frac{\mathbf{ar}}{a} \\ \nabla F &= \alpha\mathbf{r} - \beta\mathbf{r}' \end{aligned}$$

Equation (2.3) computes the magnetic field of a single dipolar source at sensor position $\mathbf{r}$. The total field of many sources is obtained by superposition, so it can also be written in form of a matrix equation. Let N be the number of sources within the volume Ω, and M the number of sensors. Then

$$\begin{pmatrix} \phi_1 \\ \phi_2 \\ \vdots \\ \phi_M \end{pmatrix} = \begin{pmatrix} L_{11} & L_{12} & \dots & L_{1N} \\ L_{21} & \ddots & & \vdots \\ \vdots & & \ddots & \vdots \\ L_{M1} & \dots & \dots & L_{MN} \end{pmatrix} \cdot \begin{pmatrix} J_1 \\ J_2 \\ \vdots \\ J_N \end{pmatrix} \tag{2.4}$$

where the vector $\mathbf{J}$ contains the dipole amplitudes of N sources located at fixed positions with given orientations. $\mathbf{L}$ denotes the leadfield matrix. It involves information about the assumed volume conductor model, the source configuration, and sensor geometry. The entries of $\mathbf{L}$ are scalar, resulting from the projection of the magnetic field vector onto the sensor normals. The n-th column of $\mathbf{L}$ reflects the field that would be measured at the M sensor locations if only the n-th source was active. ϕ is the measurement vector of the N superimposed sources.

2.4 The inverse problem

In the previous section, the issue of evaluating the magnetic field of a given source configuration has been discussed. This issue, known as the electromagnetic forward problem, has a unique solution.

Now the inverse problem of finding the underlying sources of a measured magnetic field will be tackled. This is a fairly demanding question since the inverse problem is inherently ill-posed. Even if the electric and the magnetic field everywhere outside the head were known, a unique solution for the current dipoles would not exist (Hämäläinen, 1992). A source model incorporating prior knowledge about the generators of the data, or imposing additional constraints on the solution is required to solve the electromagnetic inverse problem uniquely.

2.4.1 Dipole fitting

A very common source model is the ECD, as mentioned above. So, for estimation of the generators of MEG data, a few current dipoles with given initial positions and orientations are assumed. Based on the chosen forward model, the magnetic field of these sources is computed and compared to the measured data. Then the source parameters are altered in order to minimize the norm of the difference between the measured and the estimated field vectors.

$$\|\phi - \hat{\phi}\| \rightarrow min$$

It is a non-linear least-squares optimization problem to determine the coordinates and orientations of each dipole. Mathematically, dipole fitting implies the solution of an over-determined equation system, that means the number of unknowns has to be smaller than the number of equations. The actual number of parameters depends on the dipole model used, which can be demonstrated by the concept of the spatio-temporal dipole: A simple ECD has six parameters for each sample point in time - three position coordinates and three orientation vectors. For an interval of 100 sample

points, this are 600 parameters for the so-called *moving dipole*. The *rotating dipole* has a fixed spatial position and variable orientation, which amounts to a total of 303 parameters for the given time interval. Finally, the *fixed dipole* has three spatial and two orientational coordinates for the complete interval, and only a time-varying amplitude. This results in 105 fitting parameters.

With today's multichannel devices, the number of parameters is usually no problem. In fact, a major drawback of this method is that the number of sources has to be known before the optimization is started.

2.4.2 Distributed sources

Another approach to solve the biomagnetic inverse problem, and circumvent the question of how many sources are active, employs a distributed sources model. Here, dipoles with fixed positions and orientations are assumed everywhere in the brain, and only their amplitudes are estimated when they are activated. The dipole positions can either form a regular 3D grid with orientations parallel to the coordinate axes, or the dipoles are placed perpendicularly to the cortical surface, where the majority of MEG and EEG generators are supposed to come from.

In either case, a highly underdetermined linear equation system is involved, since the number of assumed sources N is usually much higher than the number of measurement channels M (see equation (2.4), page 19). A unique solution can only be found when additional constraints are imposed, like for example maximum-likelihood approach, minimum norm approach, or resolution optimization approach. Multiple priors can be incorporated by the Bayesian framework (Hauk, 2004).

The widely used minimum norm criterion requires the solution to best explain the data under the condition that the norm of the dipole amplitudes is minimal (Hämäläinen and Ilmoniemi, 1994). So the problem that has to be solved is the minimization of the following functional, see for example

(Mattout et al., 2006) and (Mattout et al., 2007):

$$\hat{\mathbf{J}} \;=\; min\Big\{\|\mathbf{C}^{-1/2}(\mathbf{L}\mathbf{J}-\phi)\|^2 \;+\; \lambda\|\mathbf{W}\mathbf{J}\|^2\Big\} \tag{2.5}$$

where $\mathbf{C}$ is the $M \times M$ data covariance matrix and $\mathbf{W}$ is an $N \times N$ weighting matrix, which allows larger amplitudes for deeper sources and weaker superficial sources. This is important because otherwise, due to the minimum norm criterion, shallow sources would always be the preferred solution. The regularization parameter λ tunes the relative importance of the accuracy term and the prior term (first and second part of eq. (2.5), respectively).

The general solution of the minimization problem in equation (2.5) can be expressed by equations (2.6) or (2.7).

$$\hat{\mathbf{J}} \;=\; \big[\mathbf{L}^T\mathbf{C}^{-1}\mathbf{L} + \lambda\mathbf{W}^T\mathbf{W}\big]^{-1}\mathbf{L}^T\mathbf{C}^{-1}\phi \tag{2.6}$$

$$\hat{\mathbf{J}} \;=\; (\mathbf{W}^T\mathbf{W})^{-1}\mathbf{L}^T\big[\mathbf{L}(\mathbf{W}^T\mathbf{W})^{-1}\mathbf{L}^T + \lambda\mathbf{C}\big]^{-1}\phi \tag{2.7}$$

The derivative of the functional in equation (2.5) with respect to $\mathbf{J}$ is shown in appendix A.1, and the equivalence of the solutions (2.6) and (2.7) is demonstrated in appendix A.2.

Chapter 3

Rating of trials by Subaveraging

In the course of MEG source localization, the issue of averaging over trials recurrently occurs. Although being a strong and widely used technique, averaging also involves disadvantages. This chapter is dedicated to shed light on this matter, discuss some related problems, and point out a novel method for data analysis.

Central element of the new approach is a compromise between averaging and single trial analysis. The strengths and limitations of the method are demonstrated by a series of simulations with different source configurations.

3.1 Introduction

Raw MEG data are a combination of brain activity, biological interference, and technical noise from outside. The signals that are not brain related are widely suppressed by measuring in a magnetic shielding room, filtering, and software noise cancellation. Two very common methods for the suppression of external interference are Signal-Space Projection (SSP, Uusitalo and Ilmoniemi (1997)) and Signal Space Separation (SSS, Taulu et al. (2003), Taulu and Kajola (2005)). A digital highpass filter eliminates possible baseline drifts, and by bandpass filtering the focus is put on a

certain frequency range.

The brain signals consist of spontaneous activity and, in the case of neurocognitive experiments, activity elicited by a stimulus. Spontaneous activity is ongoing and can be measured permanently and without external stimulation. Trying to separate the stimulus-related brain signals from spontaneous activity is challenging, because both originate in the brain.

Stimulus-related activity can be distinguished between evoked and induced activity. The difference is illustrated in figure 3.1.

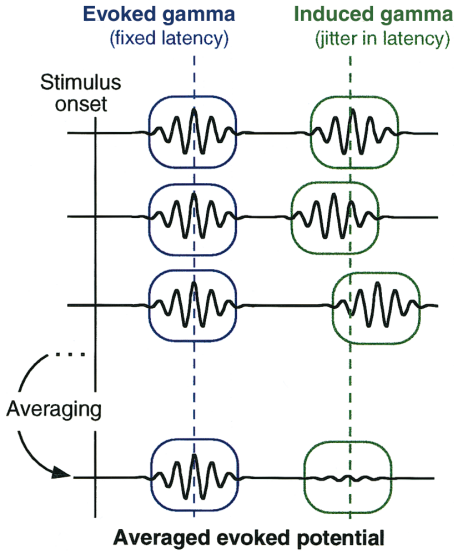

Figure 3.1: Brain responses that are phase-locked to a stimulus can be averaged. When there is a jitter in latency, averaging can completely cancel the signal. Taken from (Tallon-Baudry and Bertrand, 1999).

Evoked responses have a fixed latency and are phase-locked to a stimulus. The stimulus can either be external, presented visually or auditorily, or it can be any response of the subject, like a button press or an eye blink, for example. To compute the generators of the event-related field (ERF), averaging has proved to be useful. It is a standard procedure in data processing of many psycho-physiological MEG studies that has been applied very successfully to suppress spontaneous brain activity in favor of the evoked activity.

As can be seen in figure 3.1, induced responses have a variable latency

and are not necessarily phase-locked, so averaging them might lead to an attenuation. However, if the wave form of the brain response follows a certain temporal course, pattern search algorithms have been suggested, for example by Gath et al. (1985) or Geva and Pratt (1994).

3.1.1 Research about variability in brain signals

It has been shown that the brain does not always respond identically to repeated stimuli (Ioannides, 2001), and there is evidence that there might be a great deal of information in the data which gets lost during the averaging process. So, Ioannides (2006) argues that heavy filtering and averaging of the MEG signal might eliminate small transient activations and that raw data should be altered minimally before source reconstruction.

For example, in an MEG study about the recognition of emotional face expressions, Streit et al. (2001) found reduced ERF activity in patients with schizophrenia compared to normal subjects, and hypothesized hypoactivity in certain brain areas. Later it was shown that this reduced activation was due to higher trial-to-trial variability in patients instead of lower activation in each single trial (Ioannides et al., 2004).

An MEG study on the visual cortex examined the single trial variability of the N70m response (Laskaris et al., 2003). Checkerboard pattern stimuli of different sizes were used to elicit single trial activation dependent on the stimulus size. Different types of evoked responses were found: A large stimulus mainly induced a relative increase in brain activity time-locked to the stimulus, whereas a small stimulus lead to phase resetting of ongoing brain waves. Furthermore, the authors showed that post-stimulus brain activation is modulated by the pre-stimulus state in a non-linear way and that response variability is higher when stimuli are larger.

Not only the visual but also the somatosensory and auditory systems have been investigated on a sub-average and single trial level. An MEG study on the function of the somatosensory cortex revealed different responses in single trials to identical median nerve stimulations (Ioannides et

al., 2002). The authors employed pattern analysis to the signal power of single trials and found that the cortical responses fall into distinct clusters. Liu et al. (1998) analyzed the M100 component in an auditory mismatch negativity experiment. Focusing on the temporal features of the signals, they show that monoaural stimulation leads to earlier activation in the contralateral than in the ipsilateral hemisphere in about 2/3 of all single trials. To separate ongoing and induced brain activity, the authors defined virtual signals based on weighted averages of the real channels, which were particularly strong when the generators associated with the M100 peak were active.

3.1.2 The objective of the new method

Although some current density estimates of single trials have been computed, the primary focus of the previous studies was on the time course of the observed signals. The concern of this chapter, in contrast, aims at source localization. So, the method proposed here forms a new systematic approach to identifying neuromagnetic activation on single trial level. Preliminary results have already been presented in (Schönherr and Maeß, 2009). With numerous simulations, the following hypotheses will be tested:

1. With the subaveraging method, it is possible to determine the number of trials necessary for reliable source localization.

2. The method is able to group trials according to activated brain regions, i.e. it is possible to find out, in which trial a certain brain region was active.

The first hypothesis is tackled in section 3.4. If it is valid, the subaveraging method can provide valuable information for the planning of neuropsychological studies, since an important question in the design of these experiments concerns the number of stimuli that have to be prepared.

In section 3.5, the second hypothesis is addressed. Based on knowledge about anatomy or the experimental setup, different source models can be

tested. This means, the number and positions of assumed generators underlying the measured magnetic field can be varied. With the subaveraging method it can be investigated whether or not a single trial fits into the proposed source model.

From these investigations, far-reaching conclusions can be drawn. If there are only a few trials which do not fit into the source model, they can be regarded as noisy. It will be shown that the results improve significantly when they are rejected. If the majority of trials is not consistent with the source model, the model could be wrong. But there is a case in between, when the data set splits into parts. Many trials might be in accordance with the source model, but a considerable fraction of the data set might also show disagreement. In cognitive studies, this can happen when a subject uses different strategies to solve a task throughout the experiment. Or, in clinical context, this can be observed during the analysis of epileptic spikes. In presurgical evaluation it is of particular importance to detect the generators of these spikes exactly. The subaveraging method claims to be able to deal with different source configurations in one data set.

3.2 Random subaveraging and localization

The subaveraging method can be divided into four stages:

1. Selection of target positions
2. Random subaveraging
3. Source localization
4. Inferential statistics

1. Selection of target positions: In the very beginning one has to decide on the number and approximate positions of the sources presumably underlying the measured data. Therefore, information from previous MEG/EEG experiments of the same type can be used, as well as results

from a similar fMRI study, or simply anatomical knowledge. Any information that helps selecting target source positions is welcome.

2. Random subaveraging: Let n_t be the number of trials that contain the measured MEG signal evoked by identical stimulation of the brain. From the total number of n_t trials, subsets of n trials are considered, where $n \in \{1, 2, 5, 10, 20, 50\}$ in this thesis. For $n > 1$, n_s subsets are drawn randomly and without replacement (Hartigan, 1969), where the total amount of possibilities is limited by $\binom{n_t}{n}$. For $n = 1$, each trial occurs only once.

In the following simulations, $n_t = 200$ and if not indicated otherwise $n_s = 10000$. Experiments which are not shown here have revealed, that the results are identical when n_s is higher. In fact, since n_s should be constant for all n, it turned out that a reasonable value for n_s is about half of the upper bound which is $\binom{200}{2} = 19900$, here.

3. Source localization: The inverse problem is solved for each group of subaveraged trials ($n > 1$), and for each single trial ($n = 1$). In the examples presented in this thesis, sLORETA (Pascual-Marqui, 2002) is used. But it can be replaced by various other inverse methods, like minimum norm estimation (L2), minimum current estimation (L1), or equivalent current dipole localizations.

The distributed sources model yields a certain amplitude of activation for each location in the source space, and thus produces at least one local maximum. The local maxima are classified, where the number of classes equals the number of target positions (which have been defined in step 1). After classification, the grid point with strongest activation in each class is regarded as an estimated source position.

This procedure gives n_t solutions for $n = 1$, and n_s solutions for each value of $n > 1$. The deviations between the estimated source positions and the actual target positions form a distribution which allows inference about the source model.

4 Inferential statistics: The results are visualized in a single plot to get an impression of the whole data set. The median, the 25%, and 75% quartiles of the distance distribution are displayed as a function of n. Alternatively, separate histograms for each n display more detailed information. Deeper understanding about the source model and single trials can be derived from the figures. This will be discussed more specifically in line with the examples (sections 3.4 and 3.5).

3.3 General setup of the simulations

A series of examples will show the potentials of the method described. Therefore, simulations with an exactly known source configuration and artificial spontaneous brain activity have been performed.

The signals are constructed by a combination of two dipolar sources, which vary in position, orientation, and amplitude. They are chosen from a source space with 68424 dipoles. The dipoles form a sphere with a radius of 6 cm, a resolution of 1 mm, and are arranged in pairs with tangential orientations. This source space is also used for the inverse computations.

The pure dipole signals are contaminated by simulated spontaneous brain activity. For that purpose, a less dense source space with a grid resolution of 10 mm is built. 372 dipoles with random orientations are distributed regularly within a sphere with 6 cm radius also.

Since realistic spontaneous brain activity is assumed to be spatially and temporally correlated (Liu et al., 2010), this is also realized in the simulations. Spatio-temporal correlation is achieved by making the amplitude of dipole i at time t dependent on the mean amplitude of dipole i and its spatial neighbors (denoted by i^*) at time $t-1$. For each time instant, random numbers z from a triangular distribution are assigned to the dipoles with the arbitrary orientations. They represent their amplitude changes and are always constrained to be in the range of ± 2 nAm/ms. To ensure this range, the triangular distribution was chosen. A mathematical expression is given

in equation (3.1), where $\bar{J}_{i^*}$ indicates the mean amplitude over i^*.

$$J_i(t) \;=\; \bar{J}_{i^*}(t-1) \;+\; z \tag{3.1}$$

The simulated spontaneous brain activity is bandpass filtered at 3-30 Hz and added to the pure dipole signals. The critical filter frequencies are set to common values for the analysis of bioelectromagnetic signals. The 3 Hz highpass was chosen to ensure zero-mean for relatively short intervals in time, and the lowpass of 30 Hz covers the main frequency range used for ERF analyses. No external interference is incorporated, because as mentioned in the introduction (section 3.1), many noise reduction methods exist to suppress these. What is more, the intention is to separate between spontaneous and evoked brain activity, rather than evaluate the inverse method with respect to different noise levels.

In the following chapters the results of the different simulation experiments are presented. The first series of examples examines the spatial resolution of the described method, i.e. finding out the closest distance between two dipoles such that they can still be recognized as separate sources (section 3.4). Based on this, in the next step two dipoles are placed in a reasonable distance, and instead of simultaneous activation, they are switched on randomly. In each trial only one dipole is active, and it will be analyzed whether the dipoles can be related to the respective trials (section 3.5).

3.4 Simulation 1 - spatial resolution

Figure 3.2 displays the source positions of the first simulation series. Always two sources are active at the same time. One of them is dipole 0. It has a fixed position and points into positive z-direction. The second dipole runs through six different positions, more and more approaching dipole 0. Its orientation is either parallel or perpendicular to dipole 0, but always tangential to the sphere. In the following table, the source parameters are summarized, where α is measured between dipole 0, the center, and the respective source position (1-6). d is the Euclidean distance of each source

to position 0.

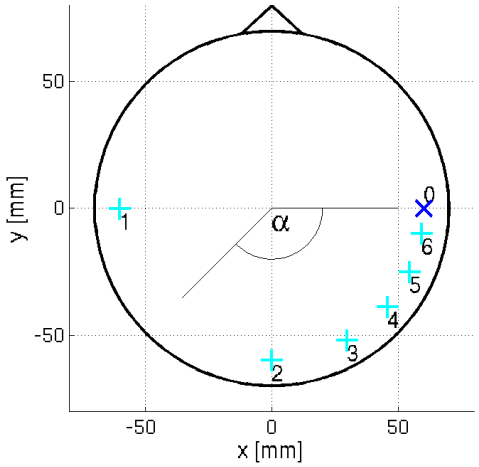

Figure 3.2: Source positions. Dipole 0 is combined with each of dipoles 1-6.

	α	x [mm]	y [mm]	z [mm]	d [mm]	orientation	amp [nAm]
0		60.0	0.0	0.2		↑	20
1	180°	-60.0	0.0	0.2	120.0	↑ →	20/10/5
2	90°	0.0	-60.0	0.2	84.9	↑ →	20/10/5
3	60°	29.7	-52.1	0.2	60.3	↑ →	20/10/5
4	40°	45.8	-38.7	0.2	41.3	↑ →	20/10/5
5	25°	54.4	-25.3	0.2	25.9	↑ →	20/10/5
6	10°	59.2	-10.0	0.2	10.0	↑ →	20/10/5

Whereas dipole 0 has a constant strength of 20 nAm, the dipoles at position 1-6 have three different amplitude values. With this setup, the results can be compared with respect to differences in

- position (i.e. distance)
- orientation
- activation strength.

The results of this first experiment series are displayed in the figures 3.3 to 3.6, as well as in appendix B.1 (figures B.1 to B.8).

Parallel dipoles, 20/20 nAm: Figures 3.3 and 3.4 show the case of parallel dipoles with equal strength. Just like dipole 0, also the second dipole is oriented into positive z-direction and has an amplitude of 20 nAm. Moving through positions 1-6, it comes closer to dipole 0 until they cannot be resolved as two distinct sources anymore. This obviously happens at position 5, as can be seen in figure 3.3.

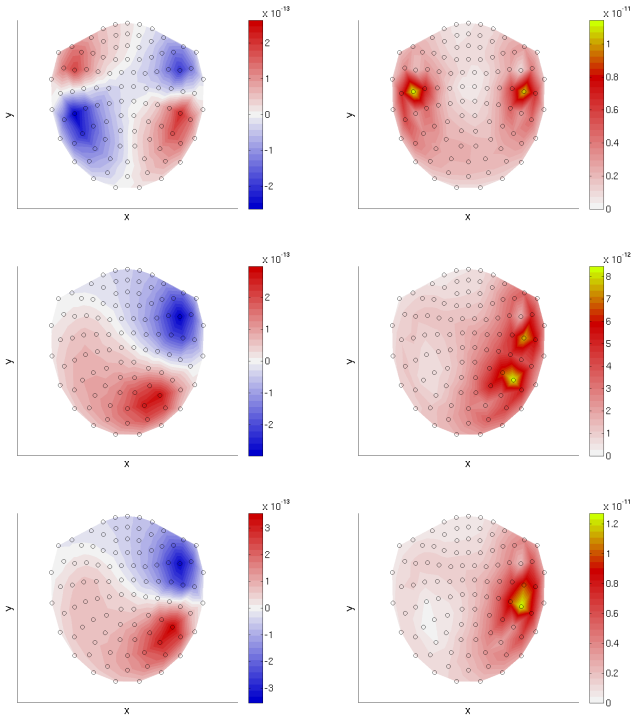

Figure 3.3: Field distribution maps for parallel dipoles with 20/20 nAm. Combinations of dipoles 1/0 (top), 4/0 (middle), and 5/0 (bottom), 200 trials averaged. Left magnetometers, right gradiometers.

The diagrams in figure 3.4 show the median and the 25% and 75% quartiles of the distribution of deviations from the target positions. For positions 1-4 the source localization results converge nicely to the targets. Although single trial localization yields significant deviations, for positions 1-3 already two, and for position 4 five randomly averaged trials yield a deviation below 1 cm with a probability of 50%.

Only at positions 5 and 6, when the distance between the sources is

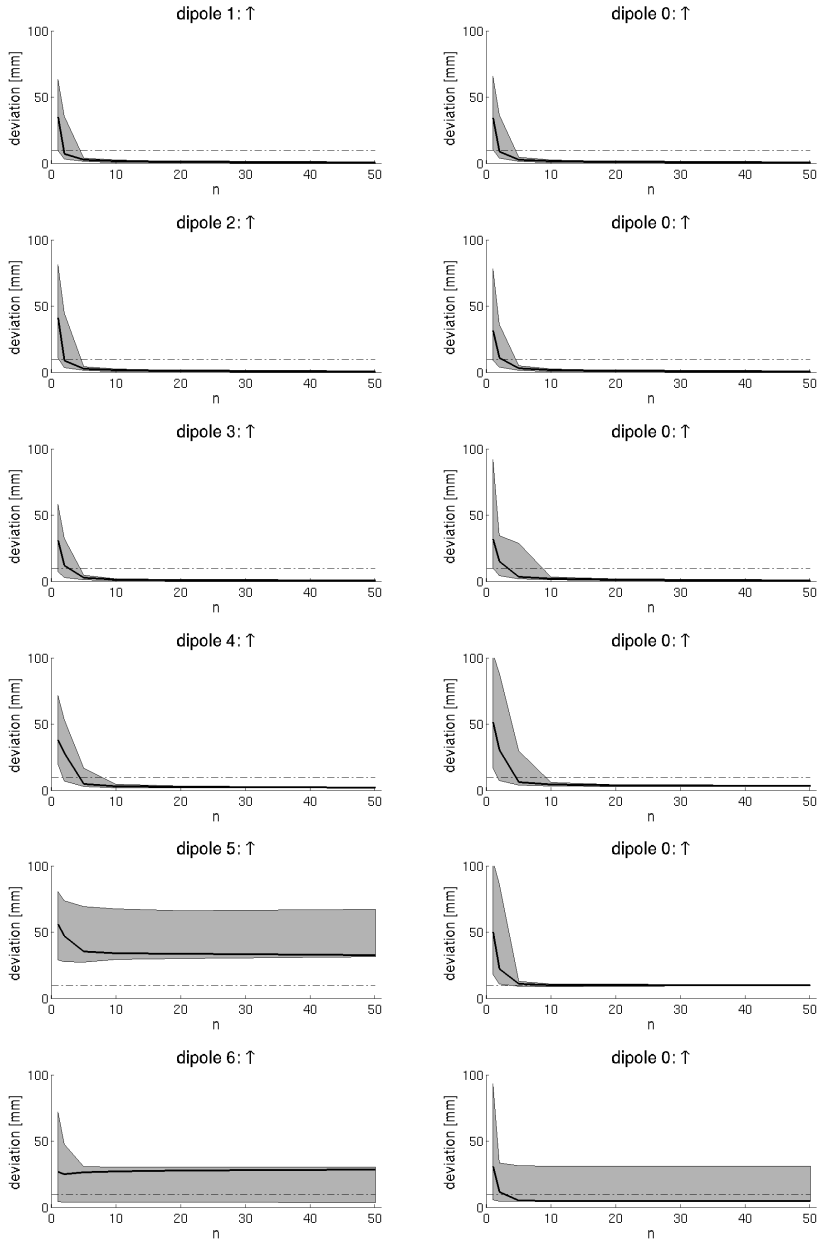

Figure 3.4: Dipoles parallel, 20/20 nAm: distribution of deviations from target positions as a function of n. The median of the distribution is drawn with a solid black line, the area between 25% and 75% quartile is shaded in gray. The dashed line at 10 mm deviation marks the deviation tolerance.

2.6 cm or smaller, source reconstruction fails. Merely one clear peak in the middle between the sources is found and classified to target position 0 (see figure 3.3, bottom). The broad distribution indicates that the other local

maxima are noisy peaks which spread all over the source space.

Perpendicular dipoles, 20/20 nAm: A similar behavior can be observed for perpendicular dipoles with equal amplitude of 20 nAm. The corresponding field maps and diagrams are shown in appendix B.1, figures B.1 and B.2. A striking difference is that source localization still works for the combination of dipoles 0 and 5. This means that dipoles in close vicinity to each other are distinguished more easily when they have different orientations.

Parallel dipoles, 10/20 nAm: Figures 3.5 and 3.6 display the results of two parallel dipoles, with 20 nAm for dipole 0 and 10 nAm for dipoles 1-6.

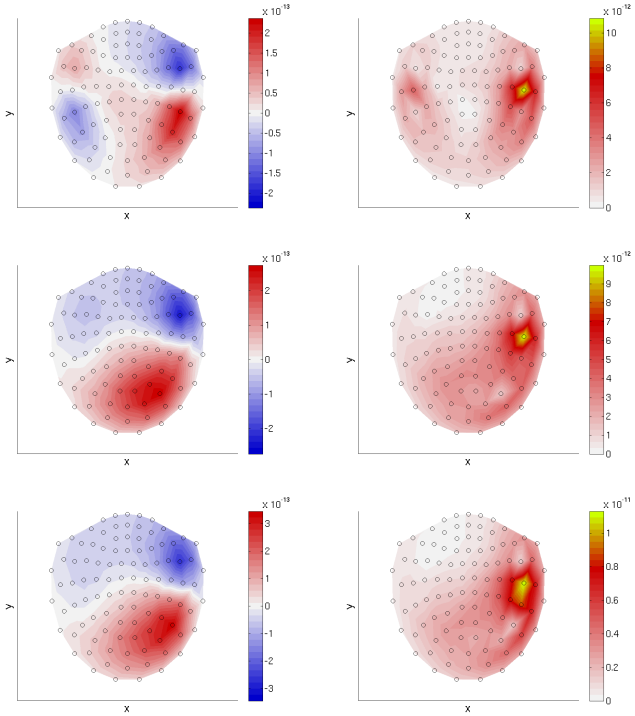

Figure 3.5: Field distribution maps for parallel dipoles with 10/20 nAm. Combinations of dipoles 1/0 (top), 4/0 (middle), and 5/0 (bottom), 200 trials averaged. Left magnetometers, right gradiometers.

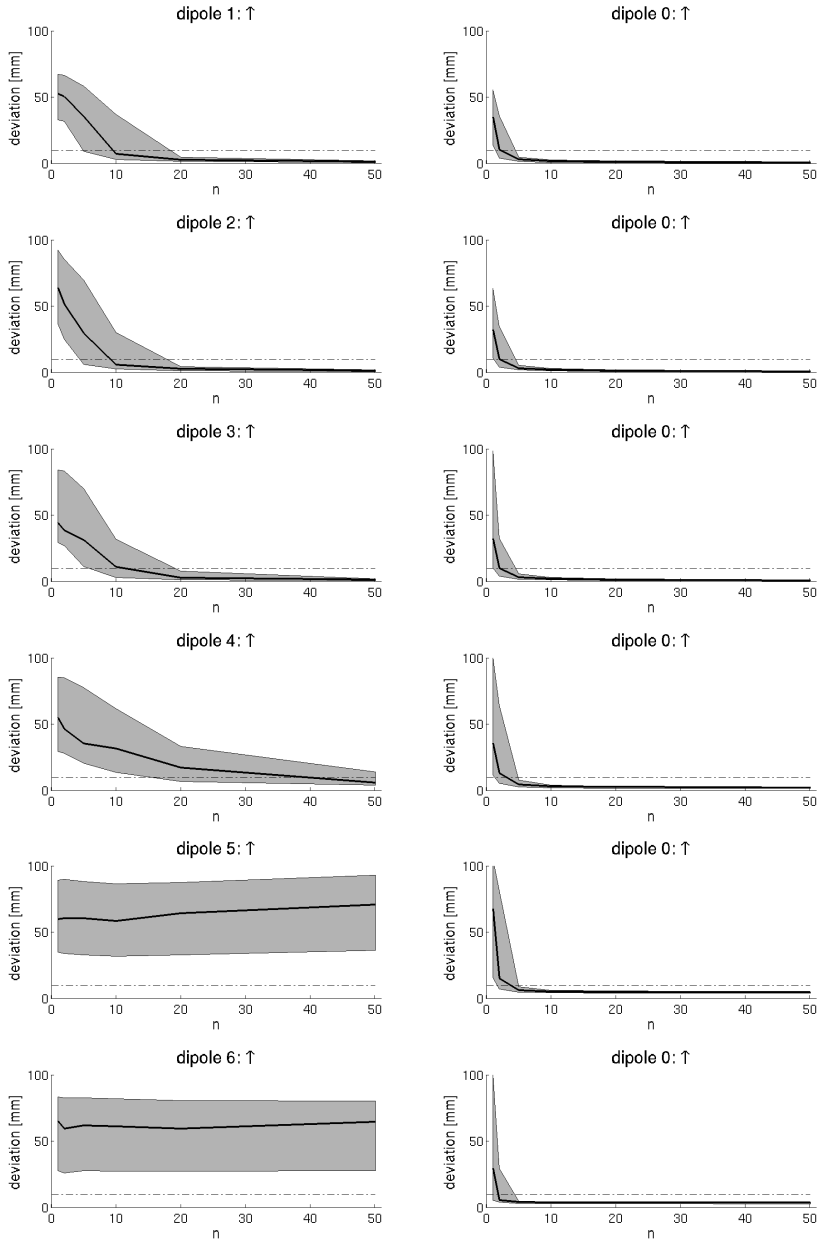

Figure 3.6: Dipoles parallel, 10/20 nAm: distribution of deviations from target positions as a function of n.

In principle, the results are comparable to those presented before. Only the results of the weaker dipole converge more slowly to the target position. Again, the results become worse, the closer the dipoles are. Although at position 4 only one peak appears in the gradiometer display (see figure 3.5, middle), source reconstruction still works for both dipoles (see figure 3.6).

However, when the second dipole is placed at position 5 or 6, only the stronger source can be found, with a slight bias towards the other source.

Perpendicular dipoles, 10/20 nAm: Figures B.3 and B.4 in appendix B.1 illustrate the results of the simulation with perpendicular dipoles, having amplitudes of 20 nAm (dipole 0) and 10 nAm (dipoles 1-6). Once more, the advantage of different dipole orientations becomes evident, as both dipoles 0 and 5 can be reconstructed. Yet, at a distance of 1 cm the weak source vanishes and only the stronger dipole is localized.

Parallel and perpendicular dipoles, 5/20 nAm: The outcome of the simulation with 20 nAm for dipole 0 and 5 nAm for dipoles 1-6 is also presented in appendix B.1. Figures B.5 and B.6 show the results for parallel dipoles, figures B.7 and B.8 for perpendicular orientations. The findings are very much consistent with those described so far. The localization results of the weak dipole converge still more slowly, whereas this dipole has essentially no influence on dipole 0. In contrast to exerting a bias to dipole 0, as in the cases before, here it is almost completely obscured at position 4 already. Again, the source is easier to localize when it is oriented perpendicular to dipole 0.

3.5 Simulation 2 - ratio variation

In the previous section, the method has been evaluated with various dipole positions, orientations, and amplitudes. It turned out, that dipoles at about 4 cm distance can be well localized, even when they are parallel but only if their amplitudes do not differ too much. For the following examination, the dipoles will have fixed parameters. They are placed at positions 0 and 4, point into positive z-direction, and both have an amplitude of 20 nAm. In figure 3.7, the source positions are visualized, the exact coordinates can be looked up in the table on page 31.

Again, the data sets are built out of a combination of the pure dipole

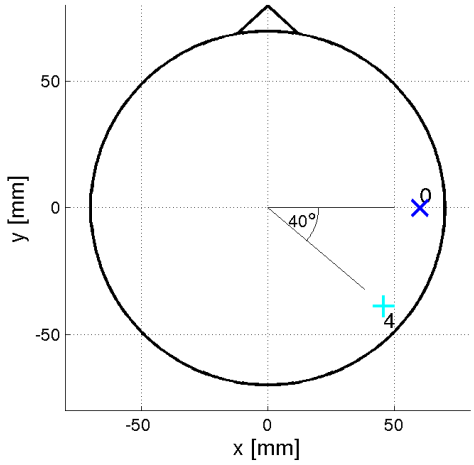

Figure 3.7: Source positions. The dipoles are parallel and have equal amplitudes of 20 nAm.

signals and simulated spontaneous brain activity. However, this time the dipoles are not simultaneously active. Rather, in each of the $n_t = 200$ trials, only one dipole is switched on. The allocation of dipoles and trials is randomized, and the ratio of the dipoles varies between 50:50 and 90:10, which is visualized in the following table.

dipole	ratio in %				
0	50	60	70	80	90
4	50	40	30	20	10

The following questions will be addressed by these simulations: How do the different ratios influence the inference about the source model? Can the ratio be discovered from the magnetic field data? Is it possible to find out in which trial which dipole was active? If so, can the source reconstruction results be improved by splitting the data set according to trials containing the same dipole?

Ratio 50:50 Figure 3.8 shows the field distribution of all averaged trials for equal proportions of both dipoles. Since the dipoles are parallel and quite close, the two sources cannot be recognized in the magnetometer map. Only the gradiometers show distinct peaks. In principle, the situation

is similar to the first example in the previous section (parallel dipoles, 20/20 nAm). But the field amplitude is reduced by factor 2, because each dipole is active in one half of the trials only. For comparison, see the field map in figure 3.3 (page 32, middle: combination of dipoles 0 and 4).

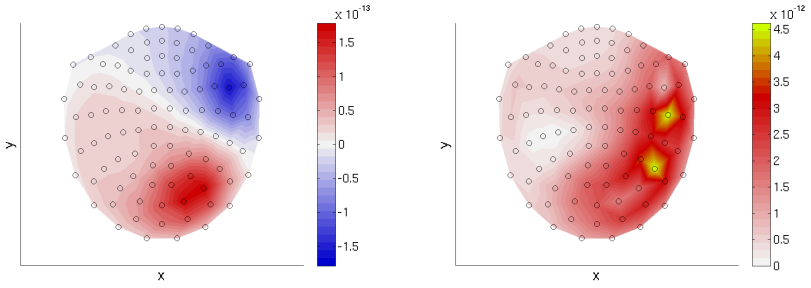

Figure 3.8: Field distribution maps for dipoles 0 and 4 (ratio 50:50). Left magnetometers, right gradiometers.

This matter of fact is also evident in figure 3.9, which depicts the outcome of the subaveraging method. The convergence behavior rather resembles that of the 10 nAm dipole in the third example of section 3.4 (parallel dipoles, 10/20 nAm; see left column of figure 3.6, page 35).

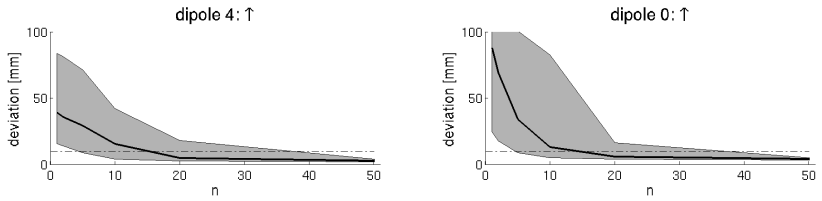

Figure 3.9: Distribution of deviations from target positions as a function of n.

So at first sight, the data would suggest a two-dipole source model, whose amplitudes would be estimated too small. However, careful analysis and a close look at the histograms reveal the actual situation. To discover that the original dipole amplitude was stronger and which dipole was active in which trial, the subaveraging method can be used with different target positions.

Therefore, instead of searching for both sources simultaneously, the

method is run two times in succession with only one target in each run. The results are presented in figure 3.10.

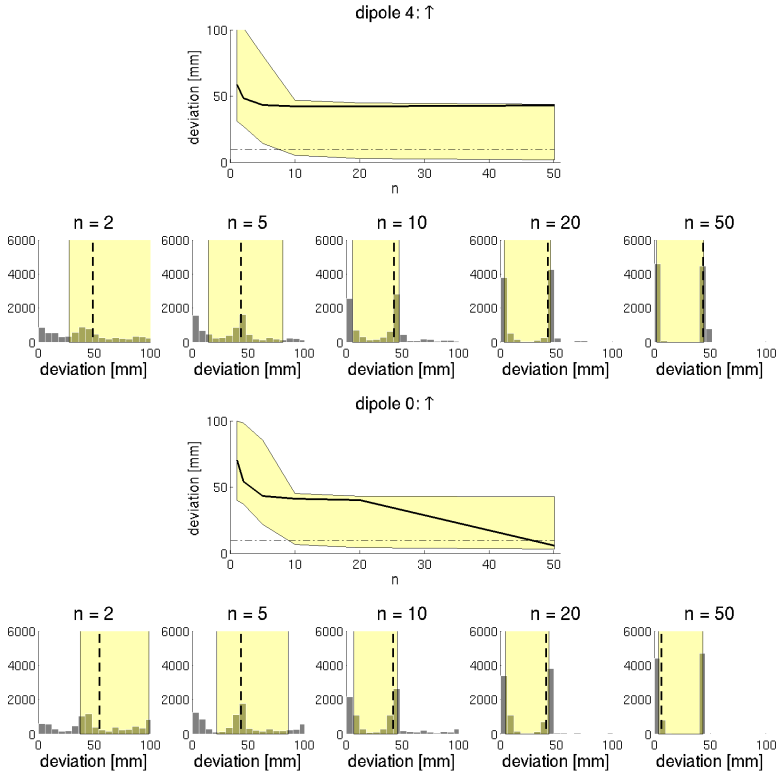

Figure 3.10: Results of the subaveraging method using target positions separately: Overall distributions and detailed display of the histograms for $n \in \{2, 5, 10, 20, 50\}$, position 4 (top), position 0 (bottom).

The histograms form sharp bimodal distributions for increasing n, with one peak at zero deviation, and another one at a deviation of 43 mm. The latter nicely corresponds to the distance between the two source positions. The equal height of the peaks indicates an equal proportion for both sources.

The next step is to find out which dipole was active in which trial. Therefore, for each n, all corresponding n_s subaverages are scrutinized. The deviation from the target position of each subaverage is assigned to the involved trials. Hence, in consideration of how often each trial occurred, the deviation of each single trial is accumulated over all subaverages. In the end those trials responsible for large deviations can be identified.

This has been done for the two target positions above, and the result is visualized in figure 3.11. The pictures show the deviation of the trials with a horizontal line that is drawn to separate 50% of the trials with the highest deviations. They do not fit into the actual source model and are marked with dark gray.

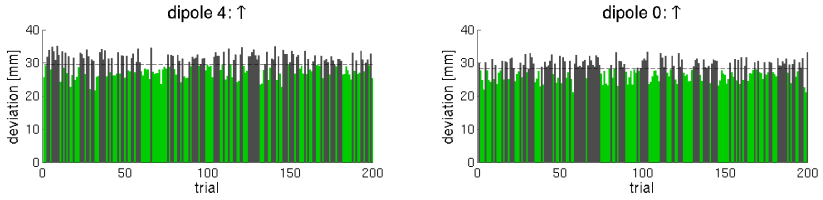

Figure 3.11: Accumulated deviation of each trial. Trials with high deviations are marked with dark gray. Hit rates are 88% for dipole 4 and 90% for dipole 0.

In the simulations everything about the sources is known, so the trial classification can be checked. It turns out that 88% and 90% of the trials have been found correctly for dipole 4 and dipole 0, respectively. 15 trials have a high deviation to both targets, which means that source localization based on them almost always fails. They are probably too noisy to extract any useful information.

As a last step, the method is run again with both targets separately. But this time only those trials are included, that have been identified to fit into the respective source model by the previous analysis. This means that all trials that are marked with dark gray in figure 3.11 are omitted for the respective target. On the left hand side of figure 3.12, the field maps of the averaged remaining trials are displayed. Now both sources are clearly visible, even in the magnetometer view.

On the right hand side of figure 3.12 the outcome of the subaveraging method is depicted. Compared to the previous results, where all trials had been used (see figure 3.10), a clear improvement can be noted. Now the distributions have only one peak and converge quickly to the target positions.

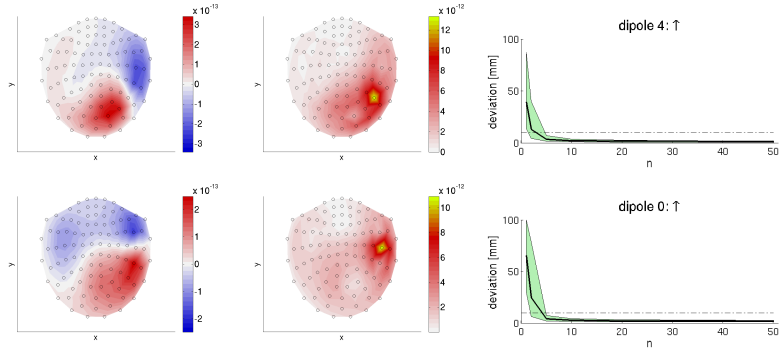

Figure 3.12: Field distributions and results of the subaveraging method after trials which do not fit into the source model have been excluded. Top row: dipole 4, bottom row: dipole 0.

Due to ignoring half of the trials, now there are fewer possibilities to find enough permutations without repetition. Thus, the number of subaverages has to be reduced, so $n_s = 4000$ here[5].

This example with 50:50 ratio of 20 nAm dipoles is very similar to a case of 10 nAm dipoles which are active simultaneously in all trials. The averaged signal would be identical, but with the subaveraging method it is possible to distinguish between the two situations. Comparing the field maps of figure 3.8 and 3.12, an increase of amplitude by factor 2 can be noted in the latter. This happens, because only those trials corresponding to the same source are picked. However, the amplitude change would not happen, if the 10 nAm data set was split into parts. It could be processed by the method in the same way, but the amplitude would stay constant.

This example shows that repetitive application of the subaveraging method can provide deep insight into the structure of a data set. Conclusions about single trials are enabled through different possibilities of analyzing and visualizing the results. This information helps improving source analysis considerably.

---

[5]The limiting value is $\binom{n_t}{2}$. For $n_t = 200$, $n_s = 10000$ subaverages were used. Since $\binom{100}{2} = 4950$, $n_s = 4000$ here.

Ratio 60:40 In the next example, the ratio is shifted from equal proportions to 60% of the trials where dipole 0 is active and 40% where dipole 4 is active. The consequence is visible in the field distributions in figure 3.13, mainly in the gradiometer map. Only the peak of dipole 0 appears, whereas the signal of dipole 4 nearly vanishes.

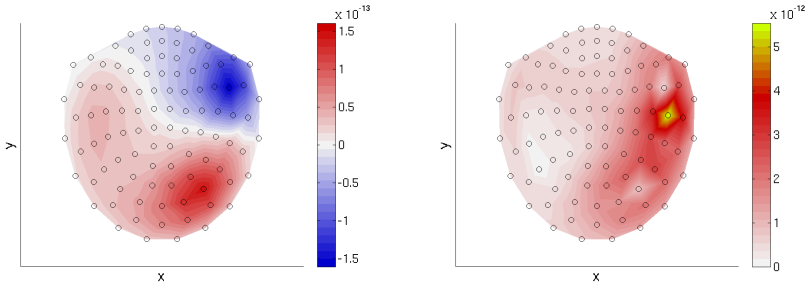

Figure 3.13: Field distribution maps for dipoles 0 and 4 (ratio 60:40). Left magnetometers, right gradiometers.

Figure 3.14 shows the result of the subaveraging method, where both targets are given. The effect of the different ratios is clearly noticeable, as the distribution of dipole 0 converges much faster than that of dipole 4.

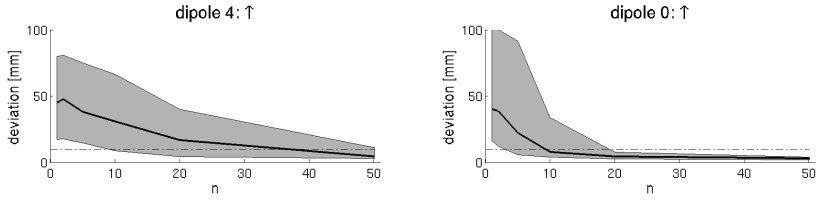

Figure 3.14: Distribution of deviations from target positions as a function of n.

However, again a deeper analysis is worthwhile to improve the convergence and distinguish trials according to the generators. So, the procedure of the example before is repeated. At first, the two sources are given as target positions in independent runs. Figure 3.15 displays the results.

Interestingly, despite the relatively high ratio of 40%, dipole 4 is impossible to localize. Still, the histograms have two peaks, but their heights are far from the 60:40 ratio. Instead, the distributions are strongly dominated

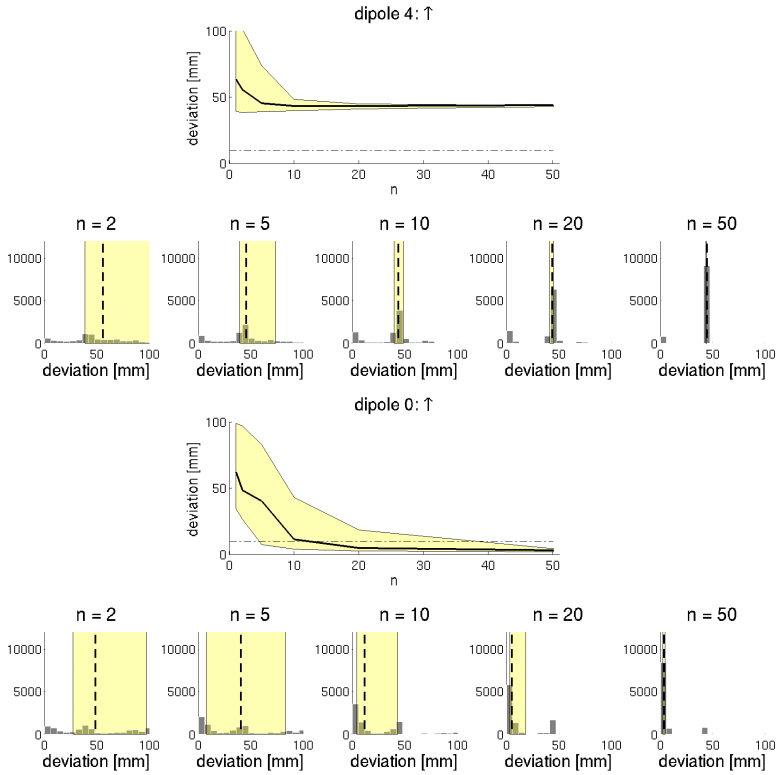

Figure 3.15: Results of the subaveraging method using target positions separately: Overall distributions and detailed display of the histograms for $n \in \{2, 5, 10, 20, 50\}$, position 4 (top), position 0 (bottom).

by dipole 0. Despite this, further analysis will reveal which trials are generated by dipole 4. Therefore, the deviations of each trial are computed and shown in figure 3.16.

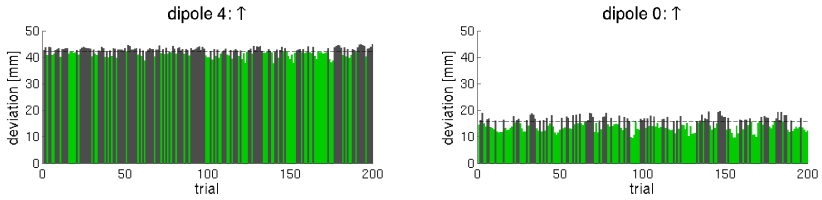

Figure 3.16: Accumulated deviation of each trial. Trials with high deviations are marked with dark gray. Hit rates are 89% for both dipoles.

The deviations from target position 4 are almost three times as high as for target position 0. This could indicate that dipole 4 is represented

in little more than 1/3 of the trials only. 89% of the trials are classified correctly to the targets. More specifically, this means that 107 trials out of 120 could be assigned to dipole 0 (60% of $n_t = 200$), and 71 out of 80 to dipole 4 (40% of $n_t = 200$). 19 trials have been found to deviate a lot from both target positions, which means that these are very noisy and not useful for source localization.

In the final step, the dark gray trials of figure 3.16 are skipped. The field maps in figure 3.17 show that again both target positions become prominent, when the respective trials are discriminated. For the subaveraging method, n_s has to be reduced even more, because in case of dipole 4, 60% of all trials are eliminated. Therefore, $n_s = 2500$ for $n \geq 2$ here[6].

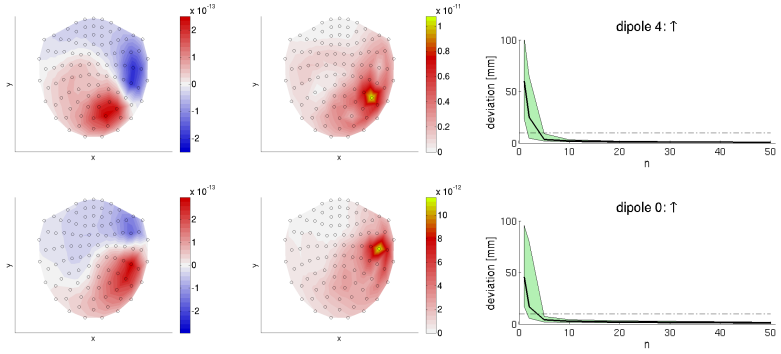

Figure 3.17: Field distributions and results of the subaveraging method after trials which do not fit into the source model have been excluded. Top row: dipole 4, bottom row: dipole 0.

The result of the method is shown on the right of figure 3.17. A nice convergence behavior for both target positions proves, that the trials generated by dipole 4 have been successfully extracted.

So the subaveraging method is very useful when trying to find sources, which are not visible in the averaged data at first sight. When from previous experiments or theoretical knowledge another source is required, the method is able to find out whether or not it is there.

[6]From 200 trials, only 80 are left. Since $\binom{80}{2} = 3160$, the number of subaverages is set to $n_s = 2500$.

Ratio 90:10 The last three examples are summarized here, because in principle they do not differ a lot. The results are discussed on the basis of the extreme ratio 90:10. In appendix B.2, the figures corresponding to the cases 70:30 and 80:20 are shown (figures B.9 to B.14, pages 98-100).

In the averaged data in figure 3.18, neither the magnetometer plot nor the gradiometer display shows a hint of source dipole 4.

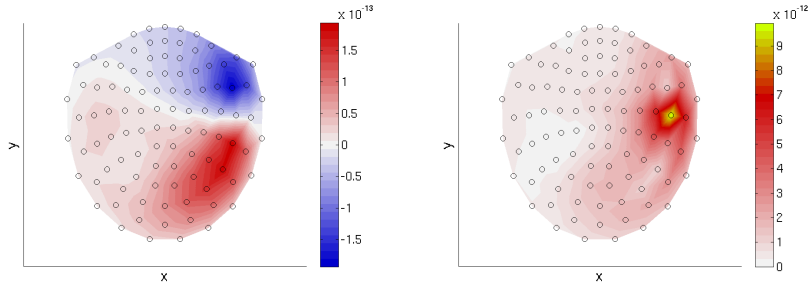

Figure 3.18: Field distribution maps for dipoles 0 and 4 (ratio 90:10). Left magnetometers, right gradiometers.

Nevertheless, both source positions are given as targets in the subaveraging method. In figure 3.19, the results are depicted. Whereas the localization results of dipole 0 converge quickly, the distribution of deviations from position 4 stays broad, even at high values of n. The median line ends clearly above the accepted distance of 1 cm, and not even the 25% quartile reaches the dashed tolerance line.

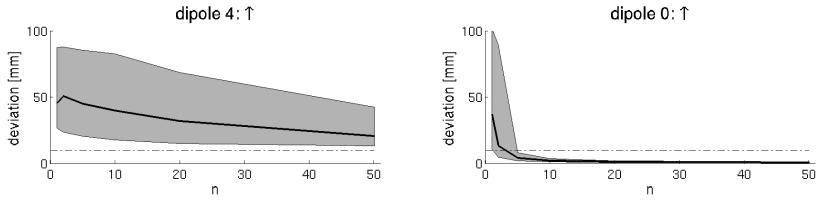

Figure 3.19: Distribution of deviations from target positions as a function of n.

With this outcome, target position 4 cannot be viewed as a real source. So the small fraction of trials that has been generated by dipole 4 is simply considered as outliers. At first, the subaveraging method is run again, solely

with target position 0. The results are displayed in figure 3.20.

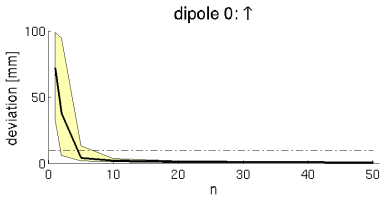

Figure 3.20: Results of the subaveraging method using target position 0 separately.

Then 10% of the trials that do not fit into this source model are excluded, and the method is rerun without them. The respective trials are marked with dark gray on the left of figure 3.21. 15 out of 20 trials (10% of 200) are found by the method correctly. The other 5 trials have a high deviation from dipole 0, although they are not generated by dipole 4. They are just noisy. On the right hand side of figure 3.21 it is demonstrated that 10% of the trials do not have an overwhelming effect. When the marked trials are excluded from further analysis, the localization results improve just very slightly (compared to figure 3.20). The impact is enhanced in the examples shown in appendix B.2.

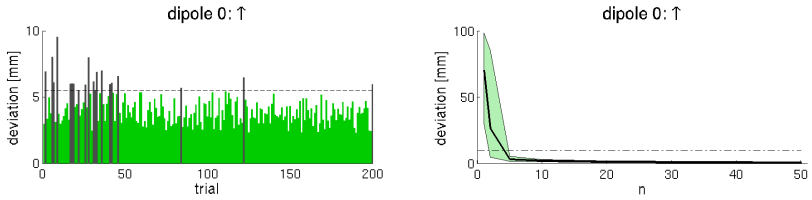

Figure 3.21: Left: Accumulated deviation of each trial. 20 trials with high deviations are marked with dark gray. Hit rate is 75%. Right: Result of the subaveraging method without the marked trials.

This example was set up such that the 20 trials generated by dipole 4 are placed in the first quarter of the data set. It imitates a real situation where a subject has to get used to a task. In the beginning of the experiment, different strategies are used. Later on, the subject decides upon one strategy to solve the task and uses it until the end. The method is able

to recognize a situation like this, where different sources might be incorporated. Trials with different strategies can be distinguished and one can focus on the dominant part.

3.6 Summary and discussion

In this chapter, the development of a novel method has been described. It is based on random subsampling and repeated source localization to enable inferences about single trials of MEG data. The variety of applications has been demonstrated by numerous examples.

By simulations, the spatial resolution with different dipole orientations and amplitudes has been investigated (section 3.4). It turned out that with the chosen source configuration and the determined sensor geometry, two dipoles with a distance of about 4 cm can be well distinguished. The distance can be diminished to 2 cm, when the dipoles have perpendicular orientations. These statements hold true, as long as the sources have almost equal amplitudes. Two additional cases have been investigated, where the ratio of dipole strength was 1:2 (10/20 nAm) and 1:4 (5/20 nAm). In the latter simulation, the weak source could hardly be reconstructed.

However, the spatial resolution is not solely determined by the dipole amplitudes and therefore by the signal-to-noise ratio. It is likely that a saturation exists, and with still higher SNR, the results would not improve anymore. Only a greater number of MEG channels could increase spatial resolution then.

Another factor is the choice of the inverse method. It was sLORETA here, which belongs to the family of minimum norm algorithms (L2). It could be possible that an L1-method which produces clearer peaks instead of smooth solutions would also lead to higher spatial resolution.

The inverse method is also relevant in regard to the noise in the data. sLORETA assumes a Gaussian noise distribution, but as described in section 3.3, the simulated spontaneous brain activity had a triangular distribution. Thus, the inverse method does not fit perfectly to the noise model,

which obviates that the localization results are too good, only because the inverse algorithm knows too much about the noise structure. Still, there is the question about how realistic the triangular distribution is. It cannot be answered conclusively, because there is no perfect model to describe individual spontaneous brain activity. If such a model existed, single trial source localization would be easier to do. So it can only be argued heuristically, that the model used here is in line with the temporal and spatial correlation mentioned in the literature (Liu et al., 2010).

Overall, it can be summarized, that both hypotheses stated in section 3.1.2 are confirmed. At normal noise levels quite few trials are sufficient to achieve good localization results with errors below 1 cm. In most examples, $n < 10$ subaverages are needed, but of course, this depends on the concrete data set.

In section 3.5, it has been described, how source localization can be even more efficient, when trials that do not fit into a proposed source model are omitted. Different cases have been analyzed and they revealed that with the subaveraging method it is possible to distinguish between data sets containing a small fraction of noisy trials, or splitting into parts, where different source models are appropriate. In this case, single trials can be attributed according to the activated brain regions.

Chapter 4

Investigations on the stability of SSS

In this chapter, the theoretical background of the Signal Space Separation (SSS) method is described. The underlying mathematical assumptions will be stated and the central formula will be derived. Then the method's stability with respect to the violation of a crucial mathematical condition is examined. Based on these findings, an extension of the applicability will be made in chapter 5.

4.1 Introduction

The idea of SSS was first introduced in 2003 (Taulu et al., 2003). A comprehensive coverage of this topic is presented in the dissertation thesis of S. Taulu (Taulu, 2008) including among others the following publications: Taulu and Kajola (2005) give a detailed technical description, and Taulu et al. (2005) provide deeper insight into geometrical issues and introduce different applications of SSS.

The method is principally based on a series expansion of the measured magnetic field in terms of orthogonal, harmonic functions. They are the essential element of the SSS basis. The entire sensor geometry is contained within this SSS basis, hence the coefficients of the series expansion provide a

device-independent representation of the magnetic field data. A very useful consequence of the functions' orthogonality is the reduced dimensionality. Thus, field information can be expressed in a compressed form, which is not possible in physical sensor space because of overlapping field components (Taulu, 2008).

A variety of applications has made this method an important and widely used tool in MEG data analysis. A complete survey of potential applications can be found in (Taulu, 2008). Here, only the most important features are mentioned and will be utilized later in this chapter and in the next.

In the first place, measured magnetic fields can be decomposed uniquely into parts originating from neuronal and environmental sources. So working as software magnetic shield, SSS enables suppression of external interference by a factor of more than 100. This is why SSS as well as its temporal extension tSSS (Taulu and Simola, 2006) have been implemented into Elekta Neuromag Oy's so-called MaxFilter^{TM} software, and now belong to the standard preprocessing routines in MEG data analysis.

Furthermore, the device-independent expansion coefficients can be combined with SSS basis functions corresponding to various sensor geometries. Therefore, MEG data can be transformed to a standardized sensor array, which is particularly useful when comparing data of different measurement sessions or data recorded with different MEG devices. In combination with continuous tracking of a subject's head position during a measurement, time-dependent standardization of MEG signals can account for head movements.

4.2 The series expansion

The derivation of the series expansion formula is based on minimal assumptions about the geometry of sources and sensors, which only require the sensors to be located in a source free volume. This is the fundamental mathematical condition mentioned above. Using the quasi-static approxi-

mation of Maxwell's equations (see section 2.3.1, equation (2.1), page 16),

$$\nabla \times \mathbf{B} \;=\; \mu_0 \mathbf{J} \quad \Rightarrow \quad \nabla \times \frac{1}{\mu_0}\mathbf{B} \;=\; \mathbf{J},$$

it follows from $\mathbf{J} = 0$ and $-\nabla \times \nabla V = 0$ that the measured magnetic field can be written as the gradient of a scalar harmonic potential.

$$\mathbf{B} \;=\; -\mu_0 \nabla V \tag{4.1}$$

The potential V of a conservative force is given by Poisson's equation which reads as follows in the electrostatic case:

$$\Delta V(\mathbf{r}) \;=\; -\frac{\rho(\mathbf{r})}{\epsilon_0}$$

In the sensor volume without any sources, where the charge density is hence zero ($\rho(\mathbf{r}) = 0$), this equation becomes homogeneous and reduces to Laplace's equation.

$$\Delta V(\mathbf{r}) \;=\; 0$$

For typical MEG sensor arrays it is convenient to solve this equation in spherical coordinates, where r denotes the radial distance, ϑ is the polar angle ($0 \leq \vartheta \leq \pi$), and φ is the azimuthal angle ($0 \leq \varphi < 2\pi$) of the sensor location. The solution of Laplace's equation in spherical coordinates is calculated in detail, for example, in (Jackson, 1982) and it is summarized in appendix C.1. The final result can be expressed as a linear combination of spherical harmonics $Y_{lm}(\vartheta, \varphi)$, which form a complete set of basic solutions of Laplace's equation.

$$V(\mathbf{r}) \;=\; \sum_{l=0}^{\infty} \sum_{m=-l}^{l} \alpha_{lm} \frac{Y_{lm}(\vartheta, \varphi)}{r^{l+1}} \;+\; \sum_{l=0}^{\infty} \sum_{m=-l}^{l} \beta_{lm} r^l Y_{lm}(\vartheta, \varphi) \tag{4.2}$$

Here, the coefficients α_{lm} and β_{lm} are the multipole moments containing the field information in compact, device-independent form and can be viewed as generalized channels. The first double-sum of equation (4.2) converges for sensor position $r \to \infty$ and diverges for $r \to 0$, i.e. it corresponds to the potential of sources that are closer to the center of the coordinate

system than the sensors. The second double-sum diverges for $r \to \infty$ and describes the potential of sources further away from the center of the coordinate system than the sensors. They will be referred to as internal and external parts in the following.

Plugging eq. (4.2) into eq. (4.1) and evaluating the gradient, the vector magnetic field is expressed as a series expansion using the modified vector spherical harmonics (VSH) $\boldsymbol{\nu}_{lm}(\vartheta,\varphi)$ and $\boldsymbol{\omega}_{lm}(\vartheta,\varphi)$. Taulu and Kajola (2005) show this step shortly, in appendix C.2 it is demonstrated in more detail.

$$\begin{aligned}\mathbf{B}(\mathbf{r}) &= -\mu_0 \sum_{l=0}^{\infty}\sum_{m=-l}^{l} \alpha_{lm} \nabla\left[\frac{Y_{lm}(\vartheta,\varphi)}{r^{l+1}}\right] - \mu_0 \sum_{l=0}^{\infty}\sum_{m=-l}^{l} \beta_{lm} \nabla\left[r^l Y_{lm}(\vartheta,\varphi)\right] \\ &= -\mu_0 \sum_{l=0}^{\infty}\sum_{m=-l}^{l} \alpha_{lm} \frac{\boldsymbol{\nu}_{lm}(\vartheta,\varphi)}{r^{l+2}} - \mu_0 \sum_{l=0}^{\infty}\sum_{m=-l}^{l} \beta_{lm} r^{l-1} \boldsymbol{\omega}_{lm}(\vartheta,\varphi)\end{aligned} \tag{4.3}$$

Transformation of the modified VSH from spherical to Cartesian coordinates (which is performed in appendix C.3) and projection onto the sensor normals $\mathbf{n}$ yields the SSS basis vectors $\mathbf{a}_{lm}$ and $\mathbf{b}_{lm}$.

$$\begin{aligned}\mathbf{a}_{lm}(\mathbf{r}) = -\mu_0 \nabla\left(\frac{Y_{lm}(\vartheta,\varphi)}{r^{l+1}}\right)|_{\mathbf{n}} &= -\frac{\mu_0}{r^{l+2}} \boldsymbol{\nu}_{lm}(\vartheta,\varphi)|_{\mathbf{n}} \\ \mathbf{b}_{lm}(\mathbf{r}) = -\mu_0 \nabla\left(r^l Y_{lm}(\vartheta,\varphi)\right)|_{\mathbf{n}} &= -\mu_0 r^{l-1} \boldsymbol{\omega}_{lm}(\vartheta,\varphi)|_{\mathbf{n}}\end{aligned}$$

Using this, a measurement vector containing the scalar magnetic field data of N channels can be written as

$$\phi([\mathbf{r}_1,\ldots,\mathbf{r}_N]^T) = \sum_{l=1}^{L_{in}}\sum_{m=-l}^{l} \alpha_{lm}\mathbf{a}_{lm} + \sum_{l=1}^{L_{out}}\sum_{m=-l}^{l} \beta_{lm}\mathbf{b}_{lm} \tag{4.4}$$

or using matrix notation

$$\phi = \mathbf{S}\mathbf{x} = \begin{bmatrix}\mathbf{S}_{in} & \mathbf{S}_{out}\end{bmatrix} \begin{bmatrix}\mathbf{x}_{in} \\ \mathbf{x}_{out}\end{bmatrix}. \tag{4.5}$$

The vectors $\mathbf{a}_{lm}$ span the space $\mathbf{S}_{in} \in \mathbb{C}^{N\times(L_{in}+1)^2-1}$, the vectors $\mathbf{b}_{lm}$ span $\mathbf{S}_{out} \in \mathbb{C}^{N\times(L_{out}+1)^2-1}$. They are the SSS basis matrices of the internal and external parts, respectively. The coefficients α_{lm} and β_{lm} are incorporated in $\mathbf{x}_{in/out} \in \mathbb{C}^{(L_{in/out}+1)^2-1\times 1}$.

In eq. (4.4), $l = 0$ is omitted because it is associated with magnetic monopoles which do not exist. The expansion is terminated at orders L_{in} and L_{out} because higher order terms would describe high spatial frequencies and fine details of the magnetic field which practically cannot be measured. First, the sensors are arranged with a certain distance, posing a limit to spatial frequency resolution due to the sampling theorem. In addition, calibration accuracy of the device is confined. Calibration includes knowledge of the exact location, orientation, and size of each sensor, the gain factor of the detector coils, and for gradiometers also balance. For these reasons, values of $L_{in} = 8$ and $L_{out} = 4$ have been suggested (Taulu et al., 2005).

$\mathbf{S}_{in}$ and $\mathbf{S}_{out}$ (i.e. $\mathbf{a}_{lm}$ and $\mathbf{b}_{lm}$, respectively) are subspaces of the entire measurement space. Although they are computed by orthogonal spherical harmonic functions, they are not orthogonal themselves. But they are linearly independent, and the angle between them depends on L_{in} and L_{out} as well as on the accurate calibration of the device. A consequence of the non-orthogonality is some overlap between the subspaces. So signals generated outside of the sensor array can also be described by the basis $\mathbf{S}_{in}$ and vice versa.

4.3 Stability of SSS-based movement correction

4.3.1 Introduction

For every series expansion, certain conditions for convergence must be fulfilled. This also holds for the expression of MEG signals in eq. (4.4). In the course of the derivation, the only assumption made was that sensors are in source-free space, such that Laplace's equation for the potential holds. This means that a spherical shell containing the sensors is needed, where no sources are allowed; similar to the annulus of convergence for the Laurent expansion of a complex valued function.

The situation is illustrated in figure 4.1. The outer radius R_{out} is the Euclidean distance between the expansion origin and the most distant sen-

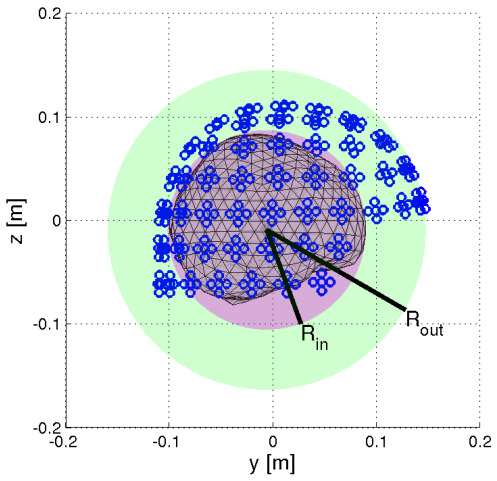

Figure 4.1: The source-free sensor volume is indicated by a green shell. Neuronal sources are enclosed by the purple sphere, external sources have to be outside of the green area.

sor. All external interference sources must be further away from the origin than R_{out}.

Here, the more crucial point is the radius R_{in}. For accurate forward modeling with a spherical volume conduction model, all neuronal sources must be closer to the origin than any of the sensors. In principle, for each realistic head position this is the case, since the head cannot penetrate the dewar. However, when transforming data between different sensor positions, the same definition of SSS coordinates is required for initial and target position. So when doing head movement correction, the center of the expansion origin needs to be optimized because in the case of extreme head movements the convergence criterion could be violated and unwanted noise effects can occur.

For example, in figure 4.2 an extreme head movement from the back to the front end of the sensor array is shown. For each individual case, an expansion origin can be found, such that the condition of a source-free sensor volume holds true. But for transformation of both head positions to a standardized sensor array, a common origin for both cases is necessary.

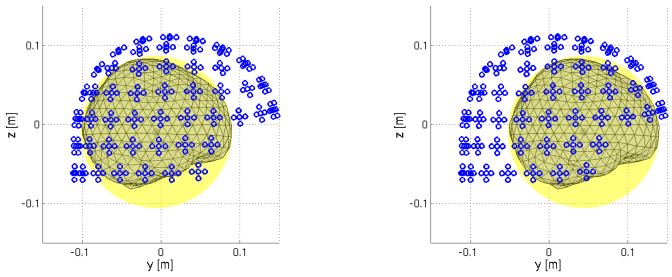

(a) (b)

Figure 4.2: Extreme head movement from (a) back to (b) front end of the sensor array. A common expansion origin cannot be found unless several sensors would also lie within the sphere and thus violate the convergence criterion.

This turns out to be a challenging, sometimes impossible task, so aim of the following investigations is to optimize the center of the series expansion and scrutinize the consequences of a violation of the convergence criterion. The results of this study have already been presented in (Schönherr et al., 2010).

4.3.2 Methods

The first step of the analysis constitutes an algorithm to find the optimized head origin. It is defined here as the center of a sphere enclosing all sources while having minimized radius, and is found based on the anatomical MRI. In principle, the choice of head origin is not that important as long as the convergence criterion is fulfilled. However, in head coordinate system, where the sources are fixed and the sensors are moving with respect to the sources, a small sphere allows for larger head movements.

The sphere should not be confused with the volume conductor mentioned in section 2.3.2. The volume conductor is necessary for accurate forward calculation, but plays no role for the SSS method. In contrast, the sphere is required for defining the expansion origin and checking the convergence criterion.

In order to imitate the violation of the convergence criterion produced

by large head movements, instead of actually moving the relative position of sources and sensors, the position of the origin is varied. It is shifted

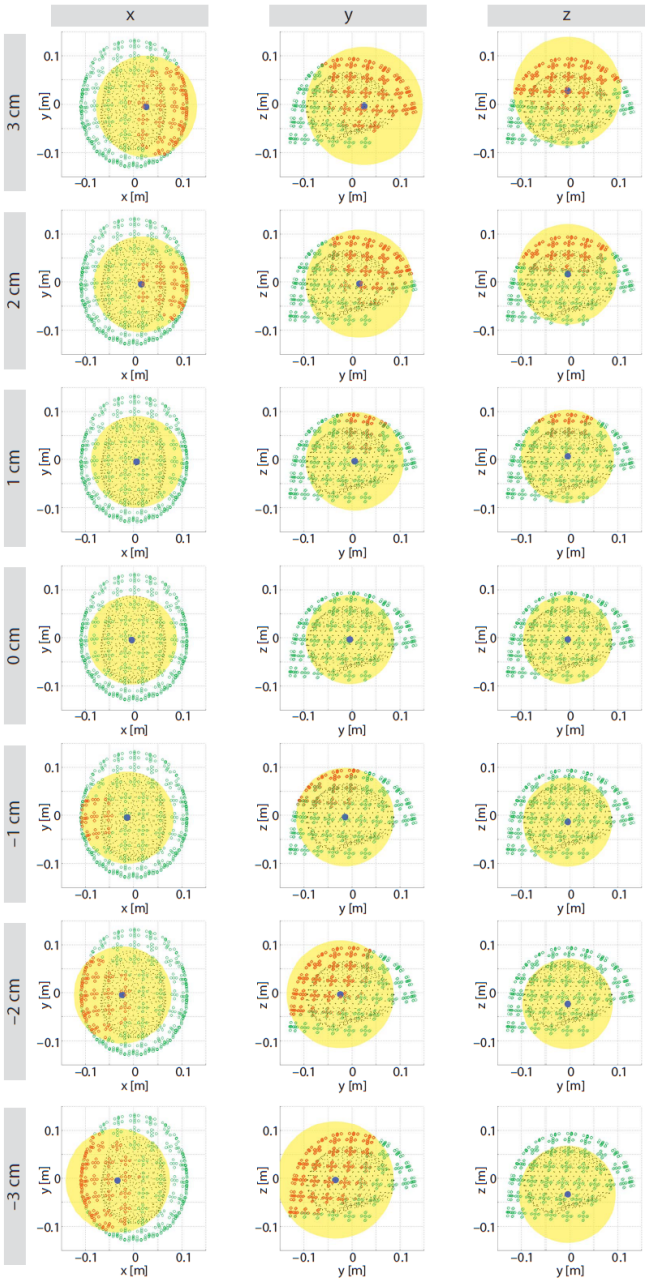

Figure 4.3: The relative position of sources and sensors is fixed. Only the position of the SSS origin is shifted by -3 cm to +3 cm along the coordinate axes with respect to the optimized origin (0 cm). Due to the different positions, different sensors violate the condition.

systematically from the optimized position along the coordinate axes, such that a sphere enclosing all sources necessarily cuts few sensors. This is shown in figure 4.3, where the inner skull and the sensor coils of an example subject are displayed. The sphere is indicated with yellow and its center by a blue dot. Sensors outside of the sphere are green, sensors that violate the convergence criterion are marked with red. Their number increases with increasing displacement, since the sphere expands in order to enclose all sources.

Three example data sets from different subjects, which were exposed to auditory, visual, and somatosensory stimulation are used (details below). For each of them, MaxFilter^{TM} (version 2.1.15) with head movement correction is applied with all 19 SSS origins. The raw data are bandpass filtered, averaged, and sources are localized using Elekta Neuromag source-modeling software (xfit program version 5.5.18). The localization results of MaxFilter^{TM}-processed data using the optimized origin provide reference source positions. By comparing the dipole fitting results of the shifted origins to those from the optimized origin, the effect of different SSS origins on source localization is examined.

Auditory Data These data are taken from a mismatch negativity (MMN) experiment, comprising a standard tone (1000 Hz) and four different deviant frequencies (1091 Hz, 1189 Hz, 1414 Hz, 2000 Hz). The stimuli had a sinusoidal profile and a duration of 50 ms including 5 ms rise and 5 ms fall time. A similar experiment has been conducted by Maeß et al. (2007), where the experimental setup is described in more detail. Inter-stimulus interval (ISI) was 0.5 s, and the tones were presented binaurally while subjects were watching a silent movie. The data were recorded at 1000 Hz sampling rate, online bandpass filtered at 0.03-330 Hz, and digitally bandpass filtered at 2-20 Hz before averaging. For the present examination, the oddball response of one subject to the large deviant condition (2000 Hz) is analyzed, using the N100 component at a latency of 100-130 ms after stimulus onset.

In figure 4.4, a gradiometer butterfly plot is displayed, where channels in the temporal regions are highlighted. The topography plot shows the field gradients within the marked time interval and the sensor locations of the regions of interest (ROIs).

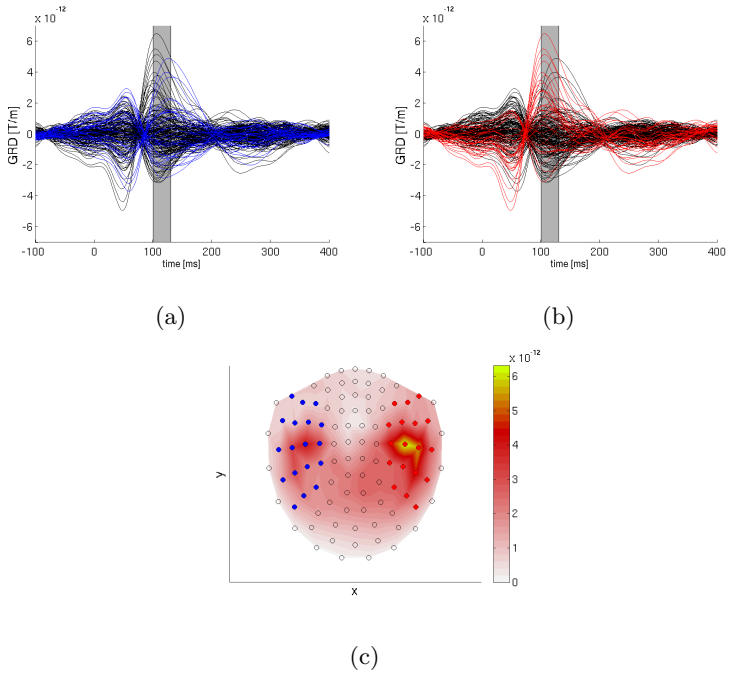

Figure 4.4: (a) and (b) Gradiometer butterfly plots of large deviant condition. (c) Gradiometer topography plot at 100-130 ms latency. Channels in the left temporal region are marked with blue, right ROI with red.

Visual Data The visual evoked field of one subject is taken from an experiment that was originally run to examine word processing. In this experiment, words were presented on a screen, and the response to correct or incorrect grammar was analyzed. For the intended purpose here, only the word onset on the screen is attended, independent of the grammar conditions. Raw data were recorded at 500 Hz sampling rate, online filtered at 0.1-160 Hz, and digitally filtered at 2-20 Hz. 40 ms time shift between the electrical trigger and the signal on the screen were taken into account. After averaging, the first visual response at the latency between 60-90 ms was analyzed (Golubic et al., 2011). Figure 4.5 shows the gradiometer

butterfly and topography plots, where a ROI was defined in the occipital region and corresponding channels are marked with green.

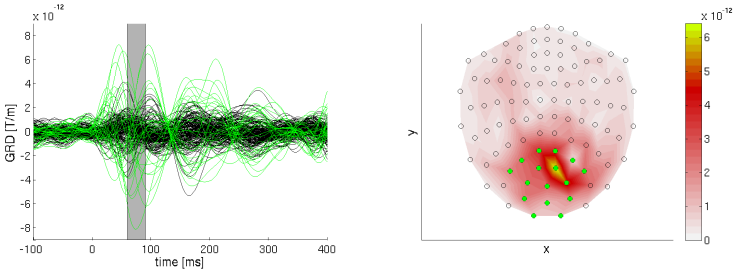

(a) (b)

Figure 4.5: (a) Gradiometer butterfly plot. (b) Gradiometer topography plot at 60-90 ms latency. Channels in the occipital region are marked with green

Somatosensory Data Somatosensory activity of one subject was induced by tactile stimulation of left and right index finger using a balloon diaphragm driven by bursts of compressed air. A detailed description of the pneumatic stimulation device is given by Mertens and Lütkenhöner (2000). For each finger, one block of about 1000 stimuli was applied with an ISI of 1 s and 10% variation to avoid habituation effects. Sampling frequency was 600 Hz, and online lowpass filtering at 200 Hz and a digital bandpass filter of 1-30 Hz were applied. The time course was corrected for the delay between the electrical trigger and the arrival of the pressure pulse, as well as the inertia of the stimulator. Mertens and Lütkenhöner (2000) report a value of 49 ms for the device, however 52 ms were used here, which has recently been measured by Lew et al. (2009). The raw data were averaged and the time interval between 35-55 ms including the peak of the first tactile component was analyzed (Lew et al., 2009). In figure 4.6, the gradiometer butterfly and topography plots for both hemispheres are displayed. ROIs have been defined and the corresponding channels are highlighted.

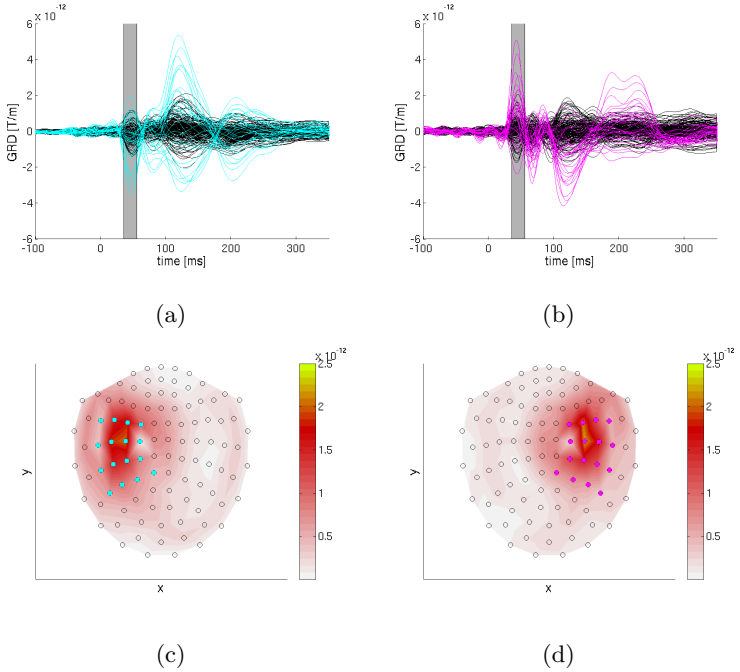

Figure 4.6: (a) and (b) Gradiometer butterfly plots of right and left index finger stimulation. (c) and (d) Gradiometer topography plots at 35-55 ms latency. Channels in the left ROI are marked with cyan, right ROI with magenta.

4.3.3 Results

Auditory Data Figure 4.7 shows the dipole fitting results, and the localization errors depending on the shift of the SSS origin for the auditory data. As expected, the dipoles localize in primary auditory cortices.

Very prominently, the largest errors occur when the origin is shifted along the x-axis. In particular, a displacement away from the dipole position increases the error, so a shift into positive x-direction raises the localization error of the dipole in the left hemisphere and vice versa. In order to avoid localization errors above 5 mm, the expansion origin should not be more than 25 mm away from its optimized position.

Regarding displacements along y- and z-axis, the errors stay below 2 mm, i.e. the results are stable with respect to these variations.

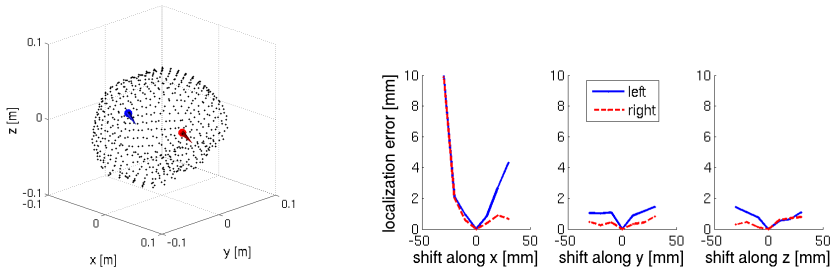

(a) (b)

Figure 4.7: Results for auditory data 100-130 ms after stimulus onset: (a) Fitted dipole positions with reference origin. (b) Localization errors for SSS origins shifted along coordinate axes.

Visual Data In figure 4.8, the result for primary visual activation is displayed. Here, shifting along the y-axis has the strongest impact, but also the x-direction has some influence on the error. Again, a displacement to the front, i.e. away from the dipole, increases the error. Also, the limit of 25 mm displacement should not be exceeded to prevent localization errors higher than 5 mm.

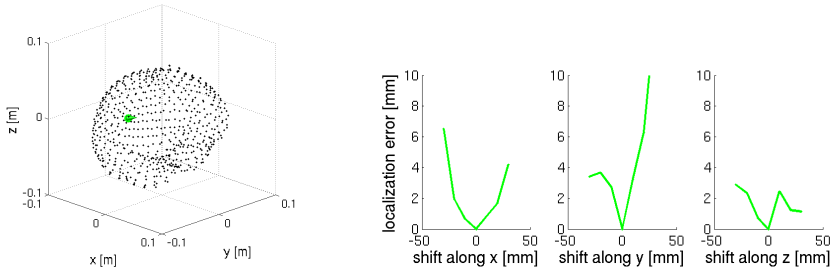

(a) (b)

Figure 4.8: Results for visual data 60-90 ms after stimulus onset: (a) Fitted dipole position with reference origin. (b) Localization errors for SSS origins shifted along coordinate axes.

Somatosensory Data The results of the somatosensory data analysis are shown in figure 4.9. In this case, both x- and z-direction play an important role, whereas the influence of y-direction is insignificant. This

indicates again a connection between dipole position and shift direction, as observed in the previous examples. Also, the 25 mm displacement threshold for localization errors below 5 mm is apparent again.

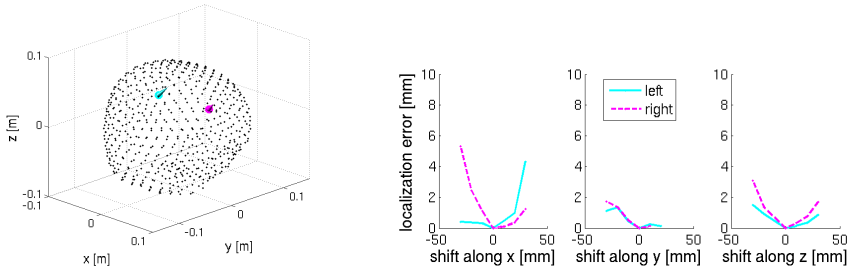

(a) (b)

Figure 4.9: Results for somatosensory data 35-55 ms after stimulus onset: (a) Fitted dipole positions with reference origin. (b) Localization errors for SSS origins shifted along coordinate axes.

In summary, a systematic increase of dipole localization errors with growing distance of the SSS origin from the reference position can be observed. The errors do not exceed 10 mm, but since they are compared to the reference origin, they accrue in addition to the inverse method's normal localization error.

4.3.4 Discussion

The SSS method appears to be rather robust against violations of the convergence criterion. Even if one third of all MEG sensors violates the condition, the localization errors are moderately small. They stay below 10 mm in all examples.

However, the noise level of sensors which violate the condition is changed, and the signal amplitudes of sensors further away from the origin become weaker. The consequence is an increasing localization error as the origin is moved away from the dipole position. This behavior was observed in all three example data sets and is demonstrated in figure 4.10. The bar graphs display the sums of gradiometer values in the respective ROIs and time intervals for different positions of the SSS origin. For the auditory and the

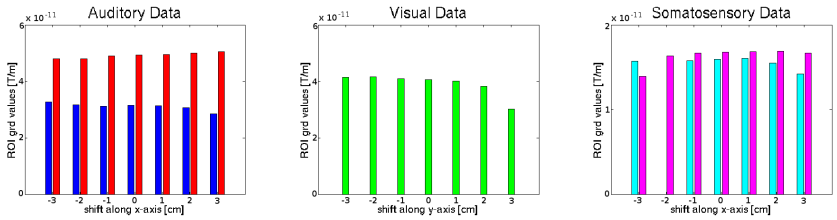

(a) (b) (c)

Figure 4.10: Bar graphs with ROI gradiometer measurements of (a) auditory, (b) visual, (c) somatosensory data for different head origins. (a) and (c) origin shifted along x-axis, (b) origin shifted along y-axis. Colors correspond to previously defined ROIs. (Somatosensory data of left hemisphere for $x = -2$ cm is not displayed, since MaxFilter^{TM} produced an error.)

somatosensory data, shift of the origin along the x-axis is shown, for visual data shift along the y-axis. Clearly visible, the amplitude of left hemisphere ROI sensors decreases when the origin is shifted to the right, and vice versa. The amplitude of measurement values in the occipital region decreases as the origin is moved to the front.

Despite the observed correlation between SSS origin and dipole localization error, the influence is very small. This source of error is not significant, compared to sophisticated forward modeling and solving the ill-posed inverse problem. So for the examined data from adult subjects there seems to be little need to carefully determine the exact position of the expansion origin based on anatomical MR images. Instead, it is sufficient to use the center of a sphere fitted to the digitized head shape, which was in all three examples less than 15 mm away from the optimized origin. This implies a dipole localization error of 2 mm at maximum, which is clearly below the tolerance value of 5 mm found at 25 mm displacement.

It should be noted, however, that during the analysis of children's data, optimizing the origin might become more important, because smaller heads are more likely to move within the dewar. So, head movements should be minimized and monitored over time to set the SSS origin in such a way that as few sensors as possible violate the condition.

Chapter 5

Transformation of MEG data

In the previous chapter, the stability of the SSS method with respect to violations of the convergence criterion has been demonstrated. It has been shown that violations have only moderate impact on the data and the criterion can be infringed to some degree. Making use of this finding, a possible extended application of SSS will be discussed in the following.

Beyond usual head movement correction, MEG data are transformed from the normal sensor positions of the device to completely new coil locations. Here, the idea is to place virtual magnetometer and gradiometer sensors directly on the scalp surface, similar to EEG electrodes. In this chapter, the benefits of this approach are investigated and the transformation results of two different methods are compared.

5.1 Introduction and motivation

The approach pursued in this chapter describes the transformation of MEG data in a way that accounts for different head shapes and sizes. The conjectured benefit of this approach is comparability of MEG data on sensor level. In EEG, this is already given to a certain extent, because the electrodes are attached to the head surface. Hence, equal electrodes have comparable positions with respect to the underlying brain areas (Koessler et al., 2009). EEG data analysis for groups of subjects is therefore often

performed on sensor level (Jensen and Hesse, 2010). The assumption is that MEG sensor space analysis (for example oscillatory or connectivity analysis) would be improved, if the sensors were located directly on the scalp surface, too. Thus, equal MEG sensors would record signals from approximately the same brain areas, in much the same way as EEG electrodes do.

Two possibilities to transform biomagnetic signals have been suggested (Wehner et al., 2008). One way is to solve the inverse problem and calculate the generators of the data. Subsequently the forward field of the reconstructed sources at the new sensors is computed. The other option relies on the multipole expansion of the magnetic field without construction of an explicit source estimate. Several studies on both transformation methods have been carried out, but no direct comparison has been performed for MEG. Here, the approaches will be considered more deeply and the results of them will be compared.

For MEG, the method based on source reconstruction has been applied by Knösche (2002). He evaluated the algorithm, transforming simulated and phantom data from individual to standard sensor positions. It turned out to be quite robust against noise, even for large differences between the sensor arrays.

Numminen et al. (1995) have also applied the first method, but in the context of MCG data. They transformed MCG signals to a standard grid form, and achieved extrapolated time courses practically identical to the original ones.

Transformation of biomagnetic fields using a multipole series expansion has been performed successfully by Burghoff et al. (1997). They have applied the technique to MCG data and transformed the recordings of different sensor types to a virtual standard sensor system. It worked well for magnetometers, first-order gradiometers with different baselines, and second-order gradiometers.

A comparison of both methods has been carried out for MCG by Burghoff

et al. (2000). They achieved good results with correlations between the signal time courses above 90%. In their investigations, the outcome of the method with source estimation involved was slightly noisier than the multipole expansion.

Whatever method was used by the authors, the target sensor array was very similar to the initial one. Coil alignment and sensor orientation were generally retained. In contrast, placing new virtual sensors directly on the head surface changes the situation significantly. The problem is that although multichannel MEG devices with more than 300 channels exist, they sample the magnetic field information rather scarcely. The vector field spreads all over, but only one direction of the flux at comparatively few locations is measured.

So, the intention of this chapter is to examine whether reasonable transformation results can be obtained for virtual target sensors on the scalp. This certainly depends not only on the sensor array but also on the sources which produce the magnetic fields. Hence, the influence of different source positions is analyzed by means of a simulation study. Furthermore, the transformation results of the two methods mentioned above are compared.

5.2 Methods

5.2.1 The simulation setup

The simulation is executed with 100 dipoles which have unit strength and random positions and orientations. They are placed inside a sphere with 7 cm radius, because according to Taulu et al. (2005) this is a typical distance for superficial sources. In figure 5.1, the dipoles are visualized by red cones. They are enclosed by the blue outer skin surface which has been obtained by segmentation and tessellation of the anatomical MRI of a human head. The original device sensor array is displayed in green, and the virtual sensor positions are indicated by black dots on the outer skin surface. They are described in further detail in section 5.3.2.

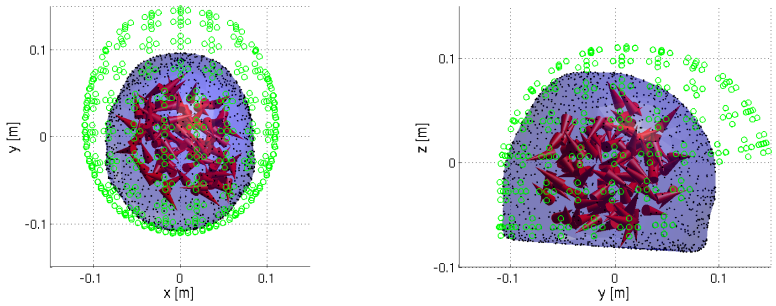

(a) (b)

Figure 5.1: Display of 100 random sources (red cones), enclosed by outer skin surface (blue) with virtual sensor positions (black dots) and device sensor array (green). (a) x-y-view, (b) y-z-view.

5.2.2 Analytical and SSS-based forward computation

Two different formulas are used to compute the forward solution for this set of dipoles. The first one is the analytical solution for the spherical volume conductor (see equation (2.3), page 18), which is called Sarvas formula in the following.

In addition, it is possible to compute MEG field distributions on the basis of the SSS series expansion. This formula is also subject to spherical symmetry, since the magnetic field is expressed in terms of spherical harmonics. It will be referred to as Taulu formula (equation (5.1), page 69).

The derivation of the forward equation based on the multipole expansion is presented by Taulu and Kajola (2005). Here, it is summarized to get a brief overview about how it works. Starting with equation (4.3) (chapter 4, page 52)

$$\mathbf{B}(\mathbf{r}) \;=\; -\mu_0 \sum_{l=0}^{\infty} \sum_{m=-l}^{l} \alpha_{lm} \frac{\boldsymbol{\nu}_{lm}(\vartheta,\varphi)}{r^{l+2}} \;-\; \mu_0 \sum_{l=0}^{\infty} \sum_{m=-l}^{l} \beta_{lm} r^{l-1} \boldsymbol{\omega}_{lm}(\vartheta,\varphi),$$

the Taulu forward equation can be derived with the following expression for the coefficients α_{lm} and β_{lm}:

$$\alpha_{lm} \;=\; \int_{\Omega} \lambda^{\alpha}_{lm}(\mathbf{r}') \cdot \mathbf{J}_{in}(\mathbf{r}') \; \mathrm{d}\Omega$$

$$\beta_{lm} \;=\; \int_{\Omega} \lambda^{\beta}_{lm}(\mathbf{r}') \cdot \mathbf{J}_{out}(\mathbf{r}') \; \mathrm{d}\Omega$$

Here, $\mathbf{J}_{in/out}$ are given dipolar sources, λ_{lm} denote lead fields, and the integration reaches over the source volume Ω.

With the vector spherical harmonic function defined by Hill (1954)

$$\mathbf{X}_{lm}(\vartheta,\varphi) \;=\; \frac{-1}{\sqrt{l(l+1)}}\left[\frac{mY_{lm}(\vartheta,\varphi)}{\sin\vartheta}\mathbf{e}_\vartheta \;+\; i\frac{\partial Y_{lm}(\vartheta,\varphi)}{\partial\vartheta}\mathbf{e}_\varphi\right],$$

the lead fields can be written as

$$\begin{aligned}\lambda^{\alpha}_{lm}(\mathbf{r}') &= \frac{i}{2l+1}\sqrt{\frac{l}{l+1}}\cdot r'^{l}\mathbf{X}^*_{lm}(\vartheta',\varphi')\\ \lambda^{\beta}_{lm}(\mathbf{r}') &= \frac{i}{2l+1}\sqrt{\frac{l+1}{l}}\cdot\frac{\mathbf{X}^*_{lm}(\vartheta',\varphi')}{r'^{l+1}}\end{aligned}$$

Now, since the forward field refers to neuronal sources, the external part is omitted and only the internal part of the equation will be considered. Using Dirac's delta distribution for a current dipole at location q, $\mathbf{J}_{in}(\mathbf{r}') = \mathbf{Q}\cdot\delta(\mathbf{r}'-\mathbf{r}_q)$, the internal multipole moment gets the form

$$\begin{aligned}\alpha_{lm} &= \int_{V'}\frac{i}{2l+1}\sqrt{\frac{l}{l+1}}\cdot r'^{l}\mathbf{X}^*_{lm}(\vartheta',\varphi')\cdot\mathbf{J}_{in}(\mathbf{r}')\;\mathrm{d}V'\\ &= \frac{i}{2l+1}\sqrt{\frac{l}{l+1}}\cdot r_q^{l}\mathbf{X}^*_{lm}(\vartheta_q,\varphi_q)\mathbf{Q}.\end{aligned}$$

This gives for the magnetic field vector the following series expansion (equation (5.1)), which is called Taulu formula here.

$$\mathbf{B}_{in}(\mathbf{r}) \;=\; -\mu_0\sum_{l=0}^{L_{in}}\sum_{m=-l}^{l}\frac{i}{2l+1}\sqrt{\frac{l}{l+1}}\cdot r_q^{l}\mathbf{X}^*_{lm}(\vartheta_q,\varphi_q)\mathbf{Q}\cdot\frac{\boldsymbol{\nu}_{lm}(\vartheta,\varphi)}{r^{l+2}} \quad (5.1)$$

Using the notation of chapter 4, it can be split into the basis matrix $\mathbf{S}_{in}$ and the corresponding coefficients $\mathbf{x}_{in}$.

$$\begin{aligned}\mathbf{S}_{in}(\mathbf{r},l,m) &= -\mu_0\cdot\frac{\boldsymbol{\nu}_{lm}(\vartheta,\varphi)}{r^{l+2}}\\ \mathbf{x}_{in}(l,m) &= \sum_{l=0}^{L_{in}}\sum_{m=-l}^{l}\frac{i}{2l+1}\sqrt{\frac{l}{l+1}}\cdot r_q^{l}\mathbf{X}^*_{lm}(\vartheta_q,\varphi_q)\mathbf{Q}\end{aligned}$$

Theoretically, the series expansion would go to infinity but it is rather terminated at L_{in} here. Examinations with real data have shown that orders $L_{in} = 8$ and $L_{out} = 4$ are sufficient for the Elekta Neuromag® device (Taulu et al., 2005). It also does not make sense to take higher orders, as explained in section 4.2. So the expansion is terminated and approximates the actual situation with a certain accuracy.

5.2.3 Two approaches to data transformation

As mentioned in the introductory section of this chapter, two methods of transforming MEG data between sensor arrays are investigated. One is based on the series expansion of the magnetic field in terms of spherical harmonic functions. The other one relies on the solution of the inverse problem and the forward calculation using the estimated sources. The methods are described more precisely in the following.

SSS-based data transformation Noise suppression and movement correction are well known applications of MaxFilter^{TM}. Especially the latter is an important feature, because the MEG sensor array is rigid and the subject's head can move relative to the sensors. This can distort the data and complicate correct source localization considerably. By monitoring the head position throughout the measurement, for each sample a new basis matrix $\mathbf{S}$ can be computed. The whole geometry information about the relative position of the head and the sensor array is contained in this basis matrix. Using equation 4.5 from chapter 4 (page 52), device-independent multipole moments $\hat{\mathbf{x}}$ are obtained by

$$\hat{\mathbf{x}} \;=\; \begin{bmatrix} \hat{\mathbf{x}}_{in} \\ \hat{\mathbf{x}}_{out} \end{bmatrix} \;=\; \mathbf{S}^{\dagger}\phi,$$

where ϕ is the vector of measured MEG data and $\mathbf{S}^{\dagger}$ denotes the pseudo-inverse of $\mathbf{S}$ (Taulu and Kajola, 2005). The multipole moments represent the series expansion coefficients and constitute an equivalent representation of the measured magnetic field data.

Noise cancellation is simply done by omitting the external part, so the biomagnetic signals are reconstructed by

$$\hat{\phi}_{in} \;= \mathbf{S}_{in}\hat{\mathbf{x}}_{in}.$$

The transformation of the MEG data to another sensor array can be realized by simply replacing $\mathbf{S}_{in}$ with a new basis matrix $\mathbf{S}^{*}_{in}$ comprising the actual or virtual new coil positions and orientations. Then the new

field vector $\hat{\phi}^*_{in}$ is computed by the product of the new basis matrix and the estimated coefficients.

$$\hat{\phi}^*_{in} = \mathbf{S}^*_{in}\hat{\mathbf{x}}_{in}$$

This transformation of MEG data to a standardized sensor configuration is the principle of SSS-based head movement correction. In this way MaxFilter^{TM} can be utilized to match MEG data recorded in different measurement sessions or on different days. Furthermore, it allows converting data between different types of detector coils, so even recordings of different devices can be compared.

Inverse and subsequent forward calculation The basis for this method is equation (2.4), page 19.

$$\phi = \mathbf{L} \cdot \mathbf{J}$$

From the combination of the current density vector $\mathbf{J}$ and the measurement vector ϕ through the leadfield matrix $\mathbf{L}$, an estimated current density $\hat{\mathbf{J}}$ can be calculated, for example, by a minimum norm algorithm (see section 2.4.2). Using a new leadfield matrix $\mathbf{L}^*$, the data vector $\hat{\phi}^*$ for different sensor positions is calculated.

$$\hat{\phi}^* = \mathbf{L}^* \cdot \hat{\mathbf{J}}$$

The source localization method employed for the computations in this chapter is eLORETA (Pascual-Marqui, 2007). It is a distributed sources approach to estimate the positions and orientations of the generators of the data. Source space is a sphere with 11476 dipoles, arranged in pairs of two orthogonal, tangential dipoles with 5 mm grid resolution. The dipoles fill the whole volume and their number is very high in order to explain the data as accurately as possible. A single sphere is used as volume conduction model.

5.2.4 Comparison of field vectors

In the following, the magnetic field vectors obtained by forward computation with the different formulas (see 5.2.2) will be termed Sarvas forward field or Taulu forward field, respectively. The field vectors computed by transformation are termed transformed field. Two different comparisons will be performed:

- comparison between Sarvas forward field and Taulu forward field (section 5.3)
- comparison between the transformed fields (by SSS-based transformation or by inverse and subsequent forward computation) and the different forward fields (Sarvas and Taulu forward fields) (section 5.4)

The first comparison shall analyze, how exactly the fields of the dipolar sources can be computed by the Taulu formula, i.e. how fast the series expansion converges towards the solution of the Sarvas formula.

In the second comparison, the results of the different transformation methods are contrasted.

For comparing the field vectors, some useful measures to quantify their similarity are required. Lew et al. (2009a) have introduced several error criteria, which are modified here a little bit in order to get meaningful values in the range between -1 and 1. They are defined as follows.

The first one is the magnification factor (MAG) indicating changes in amplitude. In principle, it is the ratio of the Euclidean norm of a vector ϕ and a reference vector ϕ_{ref}.

$$MAG \;=\; \frac{\|\phi\|}{\|\phi_{ref}\|} \;-\; 1$$

With this definition, $-1 \leq MAG < \infty$. For $MAG = 0$ both fields have equal strength, for $MAG < 0$ the reference field is stronger and vice versa.

Since the magnification factor is insensitive to differences in the topography, the second figure of merit is the relative difference measure (RDM). It computes the norm of the difference between the two normalized vectors.

It is insensitive to deviations in amplitude, but it is a very useful measure to distinguish between the topographies.

$$RDM = \frac{1}{2}\left\| \frac{\phi}{\|\phi\|} - \frac{\phi_{ref}}{\|\phi_{ref}\|} \right\|$$

It holds that $0 \leq RDM \leq 1$, so different vector orientations can be discriminated. For parallel vectors $RDM = 0$, for antiparallel vectors $RDM = 1$, and for orthogonal vectors $RDM = \sqrt{2}/2$.

5.3 Results of the forward computations

5.3.1 Original sensors

In the first part of the simulations, the forward fields of the 100 sources at the original device sensor array are computed. The Sarvas forward fields are used as reference solutions, and the results of the Taulu formula with different expansion orders L_{in} are compared to them. Figure 5.2 depicts the MAG and RDM values as a function of L_{in}. In the figure, the color coding indicates the distance of the sources to the expansion origin d_{orig}. The lines are green for $d_{orig} < 4$ cm, yellow for 4 cm $\leq d_{orig} \leq 6$ cm, and red for $d_{orig} > 6$ cm.

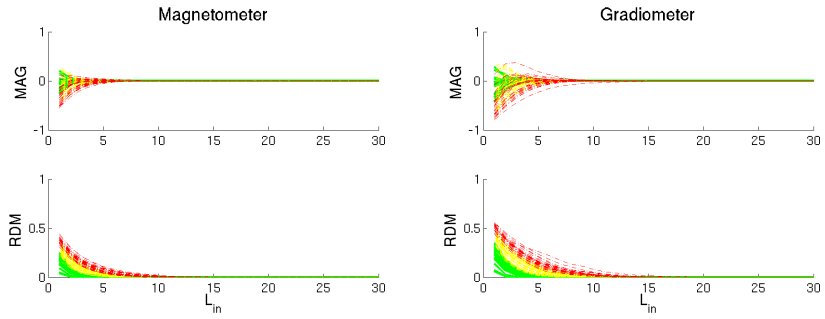

Figure 5.2: MAG and RDM values as a function of L_{in} at original device sensor positions. The distance between the sources and the origin is indicated by different colors (see text).

For all sources, the series expansion converges quite fast to the Sarvas solution. The proposed order $L_{in} = 8$ is sufficient to achieve a zero MAG

error for both sensor types. Also the RDM error is zero for sources with $d_{orig} < 6$ cm. For more superficial sources, the RDM value grows up to 0.2 at $L_{in} = 8$. For gradiometers, the errors are a bit larger than for magnetometers.

5.3.2 Virtual scalp sensors

For the definition of the virtual sensor coils it is very crucial to obey the requirement of a source-free sensor volume. The black dots in figure 5.1 (page 68) indicate the positions of 1014 magnetometers and 2028 orthogonal planar gradiometers. These positions are simply the nodes obtained from the tessellation of the outer skin surface. They are not closer than 8 cm to the expansion origin, keeping a distance of at least 1 cm between the sources and the virtual sensors. The sensor normals are radial. Due to the large amount of detector coils, a dense spatial sampling is provided.

In figure 5.3, the Taulu forward fields with different expansion orders are compared to the Sarvas fields. For the magnetometers the series expansion converges fast again. But for the gradiometers a higher expansion order is necessary for good agreement, especially for the sources corresponding to the red lines, which are more than 6 cm away from the origin. For the sources closer to the origin than 6 cm, $L_{in} = 8$ still yields an absolute MAG error below 0.1, only the RDM value rises up to 0.2.

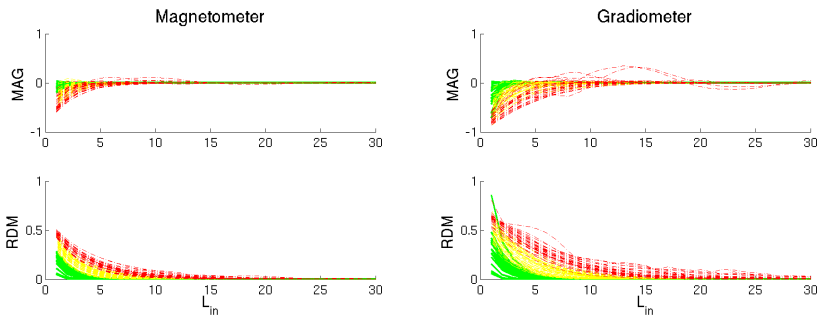

Figure 5.3: MAG and RDM values as a function of L_{in} at virtual scalp sensor positions.

The set of virtual sensors is in a comparably short distance to the brain

sources. Therefore, the magnetic field distributions produced by the nearby sources also occupy higher spatial frequencies. Consequently, the series expansion converges more slowly than for the original sensor geometry.

It is an interesting observation that the RDM and MAG errors are higher for gradiometers. This can be explained by the fact that gradiometers in principle consist of two magnetometer coils. Their values are weighted according to the baseline and combined to obtain the gradient of the magnetic field. Thus, the approximation errors of both coils accumulate and result in higher values for the gradiometers.

5.4 Results of the transformations

5.4.1 Data transformation based on SSS method

The helmet-like shape of the original sensor array covers the upper part of the head very well, but only about 60% of the full sphere (Wilson, 2004). Since the device has no coils on the bottom, there is no information available about the magnetic field there at all. Therefore, estimation of the field distribution for the lower part is avoided by constructing the virtual sensor array in a helmet-like shape as well. So, in addition to the constraint of 8 cm minimum distance to the origin, no virtual sensors on the bottom are allowed. Only nodes with $z > -0.07$ m represent virtual coil positions (see figure 5.1, page 68). Otherwise strong artifacts would occur at the respective sensors and the errors would become extremely large.

Because the simulation is done for brain sources only, the field transformation is performed based on the series expansion using $L_{in} = 8$ and $L_{out} = 0$. The transformed fields are analyzed from different points of view.

First, they are compared to the Sarvas forward fields at the virtual sensors. This reveals the difference between the computed field distribution and the one that would have been measured if it was technically possible. It shows the difference between the transformed fields and the theoretically measurable fields at the virtual sensor positions.

Second, the transformed fields are compared to the Taulu forward fields. It has been shown in the previous section (see figure 5.3), that the Taulu forward fields at $L_{in} = 8$ do not describe the field distributions on the head surface accurately enough. The results shown there imply, that data transformation from device to virtual scalp sensors goes along with an inaccuracy due to the expansion order. Since the new sensors are moved closer to the head, spatial frequencies that are initially not in the data become relevant. So, the objective of this comparison is to analyze whether the errors introduced by transformation are caused by the missing spatial frequencies alone, or if other reasons play a role, also.

In figure 5.4, the absolute MAG errors and the RDM errors of the gradiometer comparisons are visualized. As discussed above, they are considered to be more sensitive than the magnetometer errors. Therefore, they constitute a worst case scenario and provide upper limits for the errors.

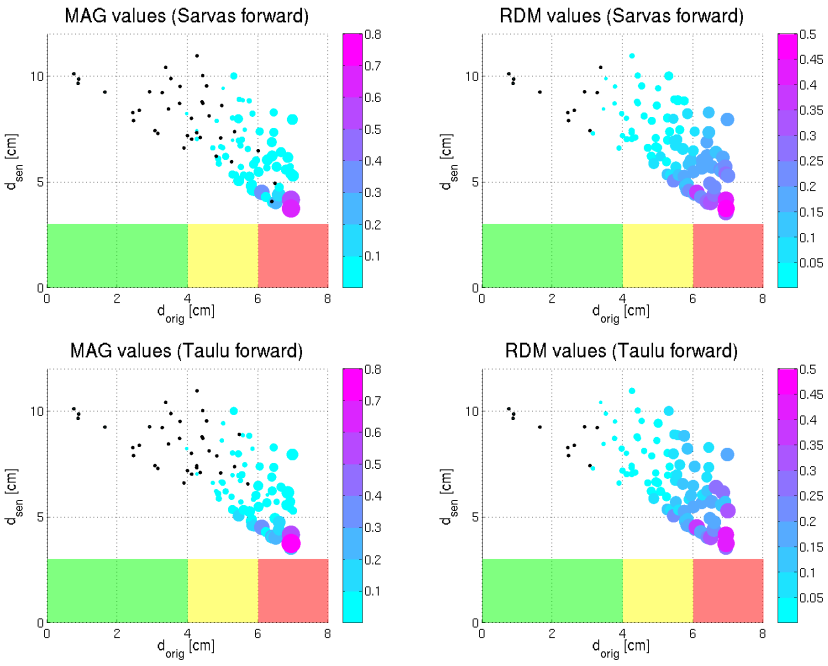

Figure 5.4: Absolute MAG and RDM errors for comparison of SSS-based transformation with Sarvas forward fields (top row) and with Taulu forward fields (bottom row). Only the gradiometer values are shown.

The values are displayed for each source as a function of its distance to the origin (d_{orig}) as well as its distance to the closest original sensor (d_{sen}). The colored bar on the bottom of each image encodes the distance between the sources and the origin, according to the colors used in figures 5.2 and 5.3. For reasons of visibility, the $|MAG|$ and RDM errors are color-coded and the dot size is scaled to be proportional to the square-root of the values. Only errors smaller than ($|MAG| < 0.0016$, $RDM < 0.0016$) are indicated by tiny black dots, because otherwise they would be invisible.

The agreement between the forward and the transformed fields of the 100 dipoles depends considerably on their position. Obviously, the transformation works very well for deep sources, close to the expansion origin, and becomes worse as d_{orig} increases. So, for $d_{orig} < 4$ cm both $|MAG|$ and RDM errors are close to zero. However, for $d_{orig} > 6$ cm they exceed 0.3 and 0.2, respectively.

But also the source positions relative to the original sensors play an important role. When the sources are more than 5 cm away from the sensors, the $|MAG|$ values are below 0.1, and the RDM errors are about 0.2. The errors become larger for decreasing d_{sen}.

These observations demonstrate that both criteria, d_{orig} and d_{sen}, have an influence on the results. So there are very superficial sources, yet far away from the closest sensor, having a smaller error than deeper sources which are closer to the sensor array.

Finally, the comparison with the different forward fields shall be considered (upper and lower row of figure 5.4). Regarding this comparison, no substantial difference can be observed. For a couple of sources, the transformed field vectors show slightly better agreement to the Sarvas forward field, reflected predominantly in the MAG errors. But there are RDM errors which are smaller for the comparison with the Taulu forward field for some sources, as well.

5.4.2 Data transformation by inverse and subsequent forward computation

Figure 5.5 depicts the results of the transformation based on source localization and forward computation using the reconstructed sources. Here, the transformed field vectors are compared to the Sarvas forward field only, because this method has nothing to do with the series expansion.

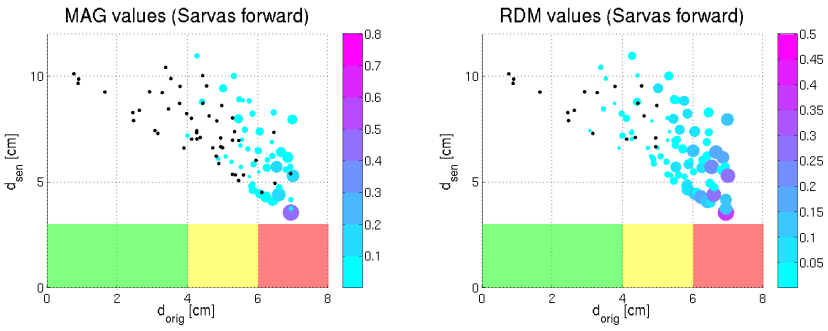

Figure 5.5: Absolute MAG and RDM values for comparison of transformation by inverse and subsequent forward computation with Sarvas forward fields. Only the gradiometer values are shown.

The general observation of the dependence on d_{orig} and d_{sen} is apparent again. But most strikingly, the agreement between the transformed and the forward fields is much better than in the previous analysis, where SSS-based transformation was used. This can be seen clearly in the absolute MAG values, which are below 0.1 for almost all sources. Only for the most superficial sources with $d_{orig} \approx 7$ cm and $d_{sen} < 4$ cm, $|MAG| > 0.4$. Also the RDM values are substantially smaller, exceeding 0.2 only sporadically for extremely shallow sources ($d_{orig} > 6$ cm).

5.5 Discussion

The investigations in this chapter described two methods for transforming MEG data from the device sensor array to virtual sensors on the scalp surface. The first method was based on expressing the measured data in terms of multipole coefficients. Using a new basis matrix containing the

geometry of the virtual sensors, the data were transformed. The second method comprised the estimation of underlying sources followed by forward computation to the new sensors. A comparison of the transformation results revealed much better agreement with the forward magnetic fields on the head surface for the second method. It is an interesting finding that the promising method which works without volume conduction modeling and inverse solution is less suitable for this application.

An explanation can be that the multipole expansion relies stronger on the actual measurements, whereas the second method is not that confined and allows more flexibility. Especially, the results shown in figure 5.4 demonstrate this. It does not make a difference which forward field is used for comparison, the transformed data just deviate a lot from the fields on the scalp. This implies that the errors are due to missing spatial frequencies that are not contained in the signals of the original sensors and thus cannot be reconstructed at the virtual sensors.

For inverse and subsequent forward calculation, the transformation does not seem to be much of a problem. Indeed, a reasonable source model is needed, and the source space has to resemble the actual simulated dipoles. This is provided by the distributed sources model, so most of the important field characteristics are mirrored by source localization. Computing new forward fields then produces really new data, and the transformation results are similar to the scalp forward fields. They are not obtained solely from the original sensor data, because through the intermediate step of source localization more information is taken into account.

These findings are in line with speculations of Numminen et al. (1995). They presumed that the poor extrapolation result of the multipole expansion method can be explained by the fact that all source current is put into a single point. The strength of the method based on source reconstruction is the realistic source current distribution.

As a general finding, which could be observed for both methods, the transformation outcome depends strongly on the source position. So the

procedure of placing virtual sensors closer to the brain is an efficient way to enhance the weak signals of deep sources. However, the signals of superficial sources should not be treated like this. By the way, this is not necessary, because the neuromagnetic signals of shallow generators are recorded well enough already. A reason for the problems with shallow sources might be that they produce strong fields with high spatial frequencies. For the series expansion, this requires large amplitudes for the higher order coefficients, which affects the whole sensor array. Changing the geometry to the virtual sensors is difficult, because the coefficients are not adjusted for it. Likewise with the source localization method, the results are biased too much toward the details of the strong fields, and pay no attention to the overall picture.

To summarize, there are a lot of constraints regarding the arrangement of the virtual sensors. When defining new sensors at really different positions, the measured field has to be extrapolated in terms of spatial as well as directional information. One tries to compute what has not been measured, and the larger the difference between initial and target sensor array, the harder and more inaccurate it becomes. This is why, the sensors have to be aligned similarly to the original sensors, regarding the helmet-like shape and normals pointing approximately into the same direction.

Moreover, one should refrain from doing source localization based on the transformed data, since the data have been obtained from measurements relatively far away from the sources. Although transformation leads to an increase in amplitude and curvature, there are still not all features recovered in the patterns that would appear in real measurements.

The objective of the examinations performed in this chapter was to study the practicability of the concept. It turned out that under certain conditions, it can be a useful tool to facilitate augmented data analysis. Based on the results here, the method of choice would be to transform the data by solving the inverse problem and not to use the SSS expansion.

First investigations with real human data have shown that the method is applicable to raw data as well as filtered or averaged data, and that the

sequence of the analysis steps does not matter. It is an interesting question whether the described data transformation could improve the detection of significant differences between conditions. This issue could be addressed with experimental data of a usual oddball design, for example. Therefore, a common definition of the virtual coil positions would be useful to have a standardized channel arrangement representing the individual head shapes, like the electrodes of an EEG cap. This could be subject of further investigations.

Chapter 6

Summary and Conclusions

6.1 Summary of the scientific results

The objective of this dissertation thesis was to evaluate existing methods and develop new approaches for data analysis in MEG. In chapter 3, a novel method has been presented which finds a compromise between averaging over all trials and single trial analysis by random subaveraging and repeated source localization. This allows drawing inferences about the generators underlying single trials of the recorded data. A systematic simulation study with a large number of examples yielded the following results.

With the subaveraging method it is possible to determine the number of trials necessary for reliable source localization for future experiments. In the depicted examples, the dependence of spatial resolution on source amplitude and orientation is illustrated. Certainly, the larger the source amplitude the higher the signal-to-noise ratio, so for stronger sources less trials are needed. The resolution of two sources in close vicinity to each other is easier when the sources have similar amplitudes, but different orientations.

Furthermore, the subaveraging method enables the attribution of single trials to certain source models. A small fraction of noisy trials can be detected and excluded from further analysis, leading to clearer source localization results. Also data sets with different underlying source config-

urations can be treated by grouping the trials according to the activated brain regions.

In chapter 4, the stability of the SSS method with respect to violations of the convergence criterion has been examined. The expansion origin was shifted systematically such that different MEG sensor coils are located within the source volume. Then the effect on source localization was investigated. It turned out that there is a strong relation between source location and shift direction. The localization errors are increasing when the expansion origin is shifted away from the source. However, the errors are relatively small. They stay below 5 mm for shifts up to 25 mm. These results are consistent throughout three different data sets. They indicate that the SSS method is stable against violations of the convergence condition requiring a source-free sensor space.

Finally, in chapter 5, two approaches for data transformation have been compared. The unconventional strategy was to convert the data to virtual sensors located directly on the scalp surface, instead of transforming between two physical sensor arrays. One of the transformation methods was based on a series expansion of the measured field in terms of spherical harmonics. The other method involved an inverse and subsequent forward calculation. For both methods, the transformation results of 100 simulated sources showed strong dependence on the source position. For deep sources far away from the sensors, the transformation is uncomplicated. Larger errors occur for superficial sources or sources too close to the sensors. The method based on source reconstruction yielded superior results compared to the method relying on the series expansion.

6.2 Conclusions and Perspective

The results of this work make a contribution to the field of MEG data processing and source analysis. Although true single trial source reconstruction still has to be regarded as an unsolved problem, more information about the generators is gained by the subaveraging method. The

usefulness of the method could be tested in the framework of more source configurations, and its applicability should be transferred from simulations to real data. Eventually, more effort in this direction is needed, and new approaches and algorithms have to be developed.

The findings made in chapter 4 are valuable, since the application of MaxFilter is a standard preprocessing step in the data analysis of many MEG experiments. A lot of published studies have shown the properties of SSS, and the present examination about its robustness is in line with these results.

The investigations on the transformation of MEG data to the scalp surface arose from an exploratory idea. As shown in chapter 5, it cannot be brought into operation naively. But being aware of the limitations, the data transformation can provide better comparability of MEG data from different subjects, or with EEG recordings.

Appendix A

Minimum norm solution

A.1 Derivation

The derivation of the general solution to the minimization problem in equation (2.5), page 21:

$$\begin{aligned}\hat{\mathbf{J}} &= min\Big\{\|\mathbf{C}^{-1/2}(\mathbf{LJ}-\phi)\|^2 \;+\; \lambda\|\mathbf{WJ}\|^2\Big\} \\ &= min\Big\{(\mathbf{LJ}-\phi)^T\mathbf{C}^{-1}(\mathbf{LJ}-\phi) \;+\; \lambda(\mathbf{WJ})^T(\mathbf{WJ})\Big\}\end{aligned}$$

$$\begin{aligned}0 &= \frac{\mathrm{d}}{\mathrm{d}J_i}\Big[\mathbf{J}^T\mathbf{L}^T\mathbf{C}^{-1}\mathbf{LJ} \;-\; \mathbf{J}^T\mathbf{L}^T\mathbf{C}^{-1}\phi - \phi^T\mathbf{C}^{-1}\mathbf{LJ} \;+\; \phi^T\mathbf{C}^{-1}\phi \;+\; \lambda\mathbf{J}^T\mathbf{W}^T\mathbf{WJ}\Big] \\ &= \frac{\mathrm{d}}{\mathrm{d}J_i}\left[\sum_{k=1}^{N}\sum_{l=1}^{N} J_k(\mathbf{L}^T\mathbf{C}^{-1}\mathbf{L})_{kl}J_l\right] \\ &\quad - \frac{\mathrm{d}}{\mathrm{d}J_i}\left[\sum_{k=1}^{N} J_k(\mathbf{L}^T\mathbf{C}^{-1}\phi)_k\right] \;-\; \frac{\mathrm{d}}{\mathrm{d}J_i}\left[\sum_{k=1}^{N}(\phi^T\mathbf{C}^{-1}\mathbf{L})_k J_k\right] \\ &\quad + \lambda\frac{\mathrm{d}}{\mathrm{d}J_i}\left[\sum_{k=1}^{N}\sum_{l=1}^{N} J_k(\mathbf{W}^T\mathbf{W})_{kl}J_l\right]\end{aligned}$$

$$
\begin{aligned}
0 \;=\; & \left[\sum_{k=1}^{N}\sum_{l=1}^{N}\delta_{ik}(\mathbf{L}^T\mathbf{C}^{-1}\mathbf{L})_{kl}J_l \;+\; \delta_{il}(\mathbf{L}^T\mathbf{C}^{-1}\mathbf{L})_{kl}J_k\right] \\
& - \left[\sum_{k=1}^{N}\delta_{ik}(\mathbf{L}^T\mathbf{C}^{-1}\phi)_k\right] \;-\; \left[\sum_{k=1}^{N}\delta_{ik}(\phi^T\mathbf{C}^{-1}\mathbf{L})_k\right] \\
& + \;\lambda\left[\sum_{k=1}^{N}\sum_{l=1}^{N}\delta_{ik}(\mathbf{W}^T\mathbf{W})_{kl}J_l \;+\; \delta_{il}(\mathbf{W}^T\mathbf{W})_{kl}J_k\right] \\
=\; & 2\cdot(\mathbf{L}^T\mathbf{C}^{-1}\mathbf{L})\mathbf{J} \;-\; 2\cdot\mathbf{L}^T\mathbf{C}^{-1}\phi \;+\; 2\lambda(\mathbf{W}^T\mathbf{W})\mathbf{J} \\
=\; & \left[\mathbf{L}^T\mathbf{C}^{-1}\mathbf{L}+\lambda\mathbf{W}^T\mathbf{W}\right]\mathbf{J} \;-\; \mathbf{L}^T\mathbf{C}^{-1}\phi
\end{aligned}
$$

$$
\hat{\mathbf{J}} \;=\; \left[\mathbf{L}^T\mathbf{C}^{-1}\mathbf{L}+\lambda\mathbf{W}^T\mathbf{W}\right]^{-1}\;\mathbf{L}^T\mathbf{C}^{-1}\phi
$$

A.2 Equivalence

Equivalence of equations (2.6) and (2.7), page 22

$$
\left[\mathbf{L}^T\mathbf{C}^{-1}\mathbf{L}+\lambda\mathbf{W}^T\mathbf{W}\right]^{-1}\mathbf{L}^T\mathbf{C}^{-1} \;=\; (\mathbf{W}^T\mathbf{W})^{-1}\mathbf{L}^T\left[\mathbf{L}(\mathbf{W}^T\mathbf{W})^{-1}\mathbf{L}^T+\lambda\mathbf{C}\right]^{-1}
$$

$$
\begin{aligned}
\mathbf{L}^T\mathbf{C}^{-1} \;=\; & \mathbf{L}^T\mathbf{C}^{-1}\mathbf{L}(\mathbf{W}^T\mathbf{W})^{-1}\mathbf{L}^T\left[\mathbf{L}(\mathbf{W}^T\mathbf{W})^{-1}\mathbf{L}^T+\lambda\mathbf{C}\right]^{-1} \\
& +\; \lambda\mathbf{W}^T\mathbf{W}(\mathbf{W}^T\mathbf{W})^{-1}\mathbf{L}^T\left[\mathbf{L}(\mathbf{W}^T\mathbf{W})^{-1}\mathbf{L}^T+\lambda\mathbf{C}\right]^{-1} \\
=\; & \mathbf{L}^T\mathbf{C}^{-1}\mathbf{L}(\mathbf{W}^T\mathbf{W})^{-1}\mathbf{L}^T\left[\mathbf{L}(\mathbf{W}^T\mathbf{W})^{-1}\mathbf{L}^T+\lambda\mathbf{C}\right]^{-1} \\
& +\; \lambda\mathbf{L}^T\mathbf{C}^{-1}\mathbf{C}\left[\mathbf{L}(\mathbf{W}^T\mathbf{W})^{-1}\mathbf{L}^T+\lambda\mathbf{C}\right]^{-1} \\
\mathbf{1} \;=\; & \left[\mathbf{L}(\mathbf{W}^T\mathbf{W})^{-1}\mathbf{L}^T \;+\; \lambda\mathbf{C}\right]\;\left[\mathbf{L}(\mathbf{W}^T\mathbf{W})^{-1}\mathbf{L}^T+\lambda\mathbf{C}\right]^{-1} \\
=\; & \mathbf{1}
\end{aligned}
$$

Appendix B

Random subaveraging

B.1 Results of simulation 1: spatial resolution

The results of the first simulation series are discussed in section 3.4. Here, only the figures are displayed for illustration.

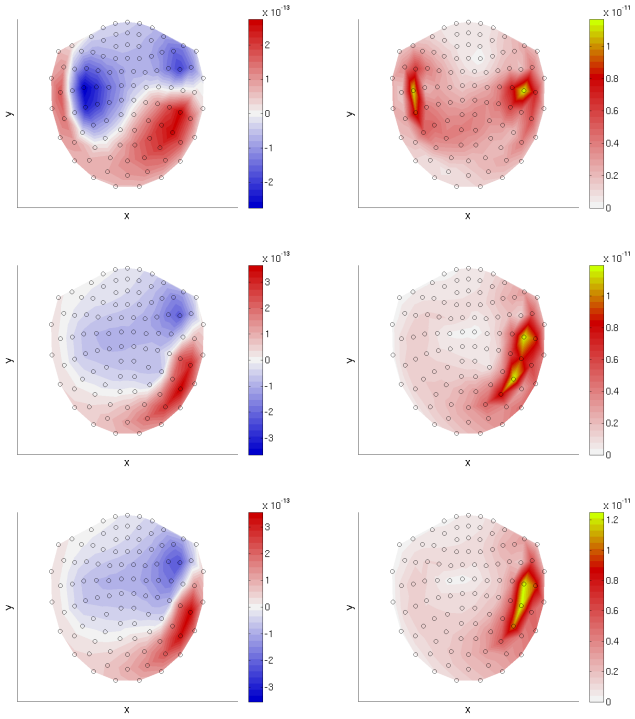

Figure B.1: Field distribution maps for perpendicular dipoles with 20/20 nAm. Combinations of dipoles 1/0 (top), 4/0 (middle), and 5/0 (bottom), 200 trials averaged. Left magnetometers, right gradiometers.

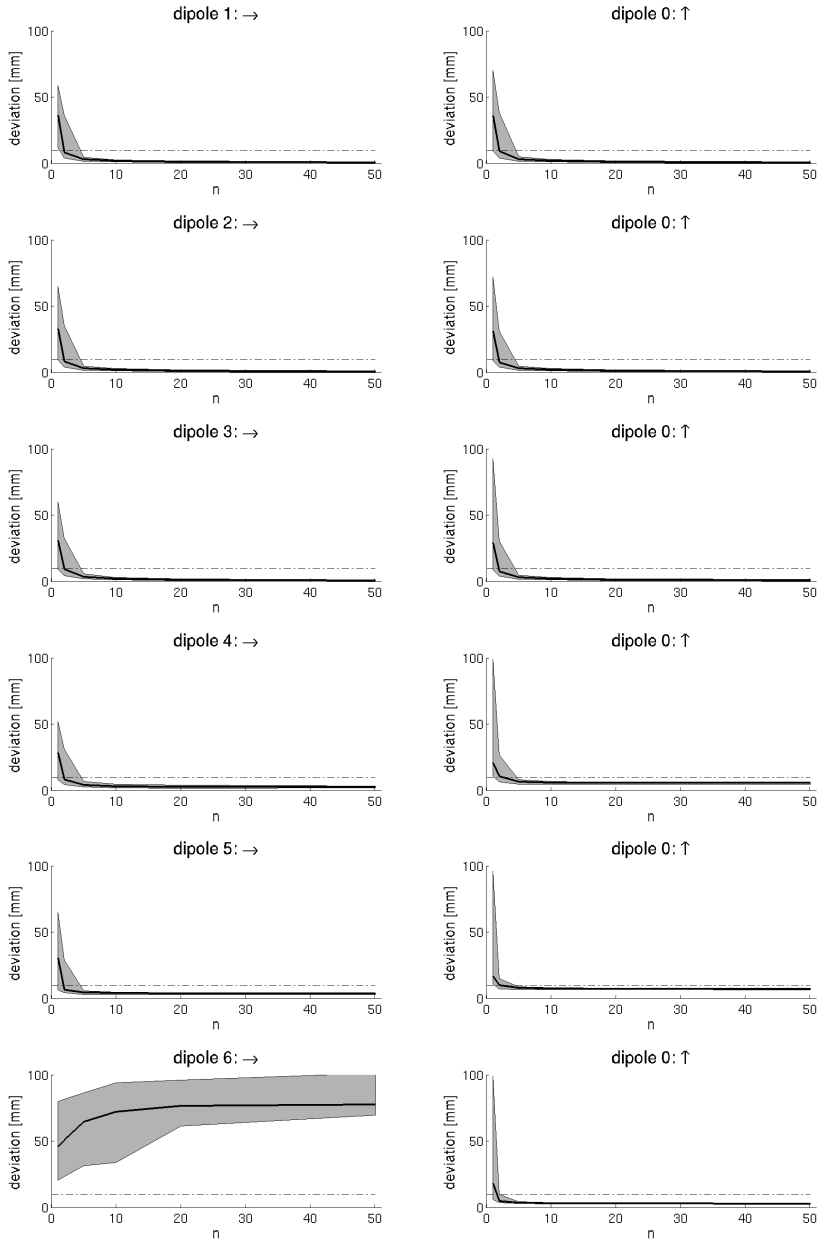

Figure B.2: Dipoles perpendicular, 20/20 nAm: distribution of deviations from target positions as a function of n.

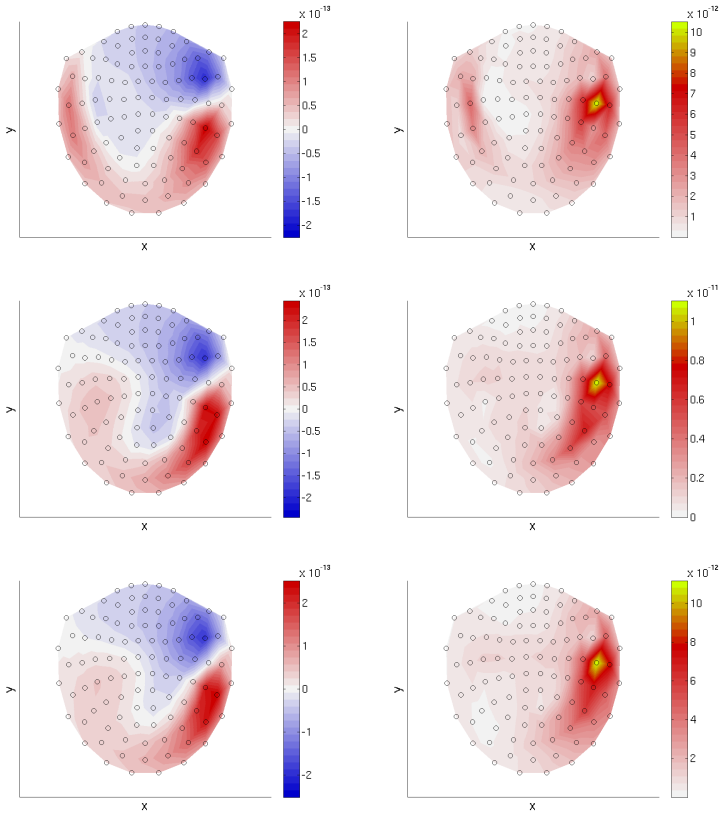

Figure B.3: Field distribution maps for perpendicular dipoles with 10/20 nAm. Combinations of dipoles 1/0 (top), 4/0 (middle), and 5/0 (bottom), 200 trials averaged. Left magnetometers, right gradiometers.

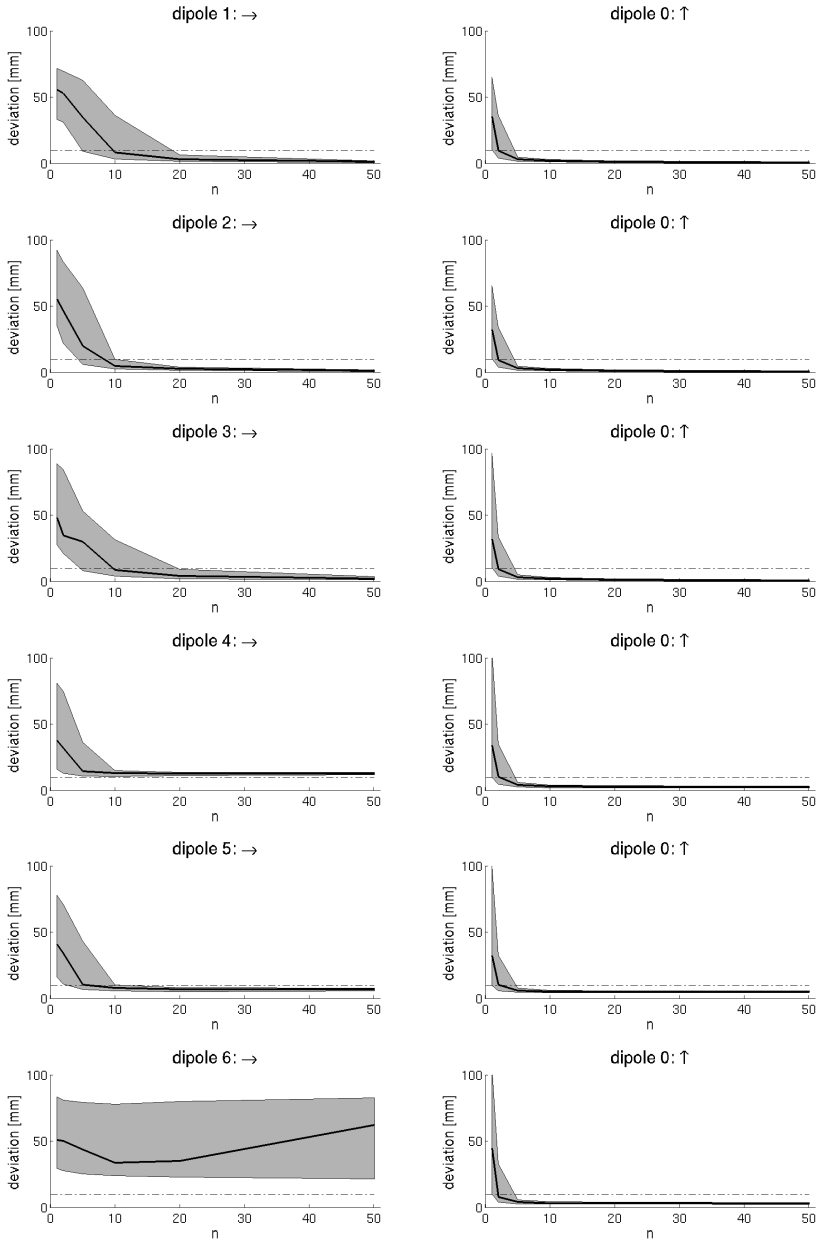

Figure B.4: Dipoles perpendicular, 10/20 nAm: distribution of deviations from target positions as a function of n.

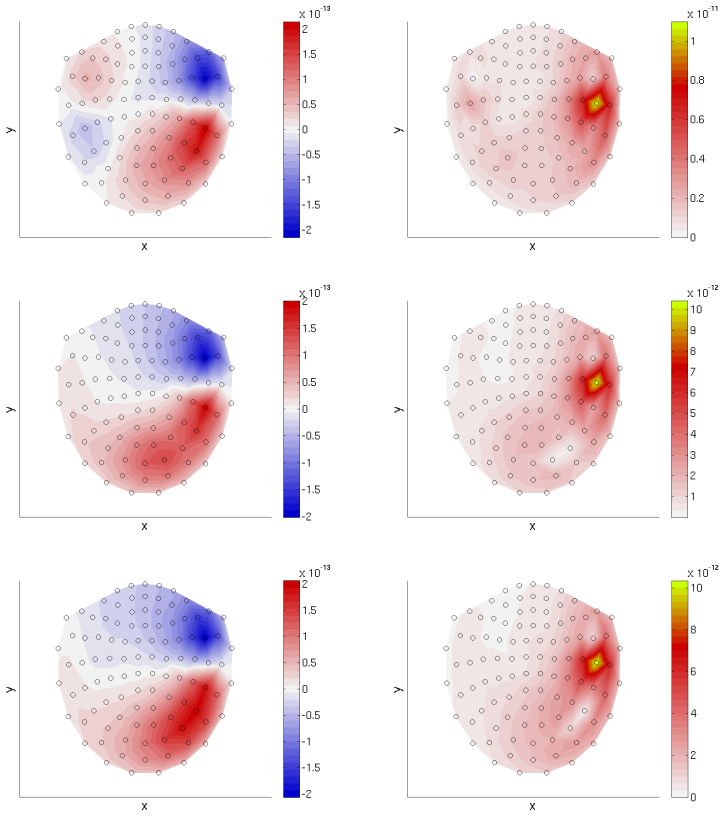

Figure B.5: Field distribution maps for parallel dipoles with 5/20 nAm. Combinations of dipoles 1/0 (top), 3/0 (middle), and 4/0 (bottom), 200 trials averaged. Left magnetometers, right gradiometers.

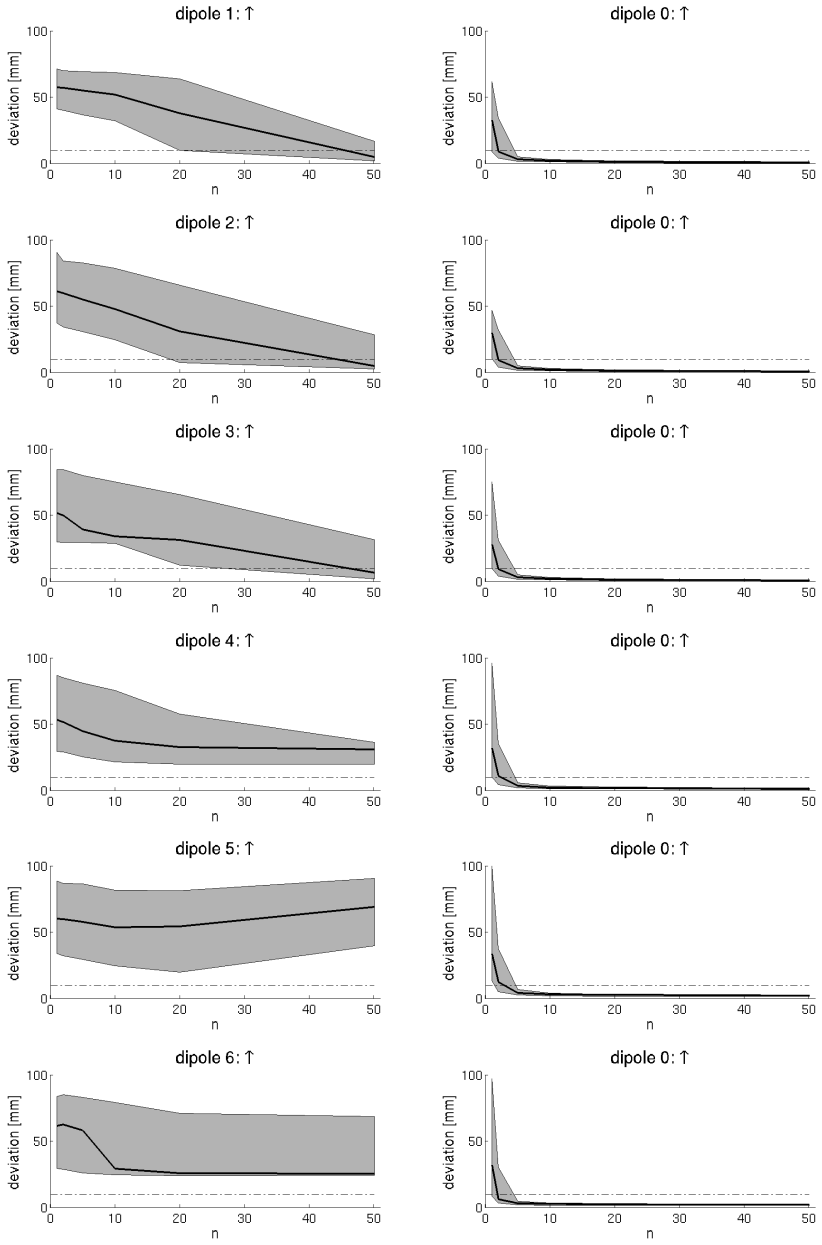

Figure B.6: Dipoles parallel, 5/20 nAm: distribution of deviations from target positions as a function of n.

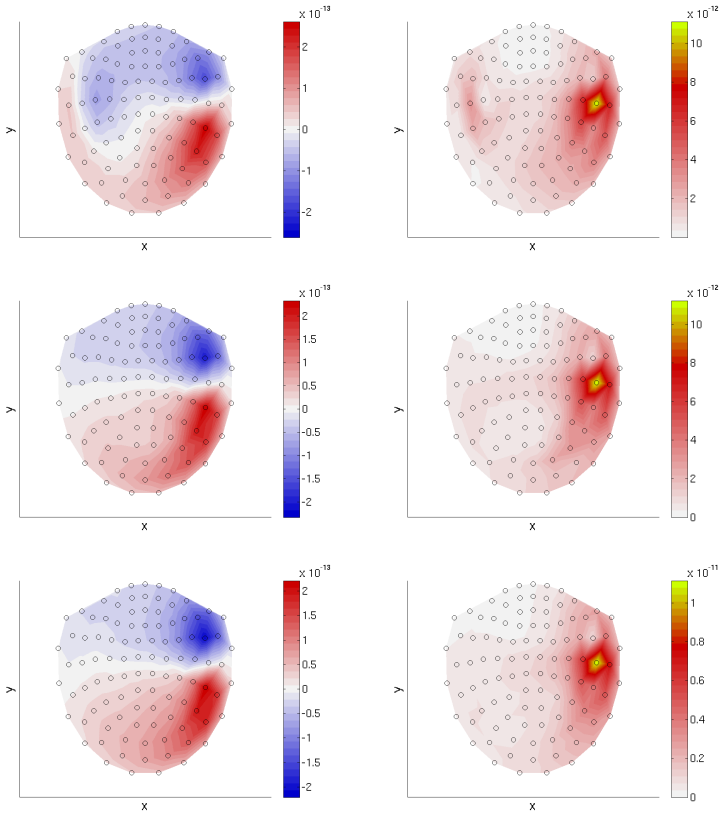

Figure B.7: Field distribution maps for perpendicular dipoles with 5/20 nAm. Combinations of dipoles 1/0 (top), 3/0 (middle), and 4/0 (bottom), 200 trials averaged. Left magnetometers, right gradiometers.

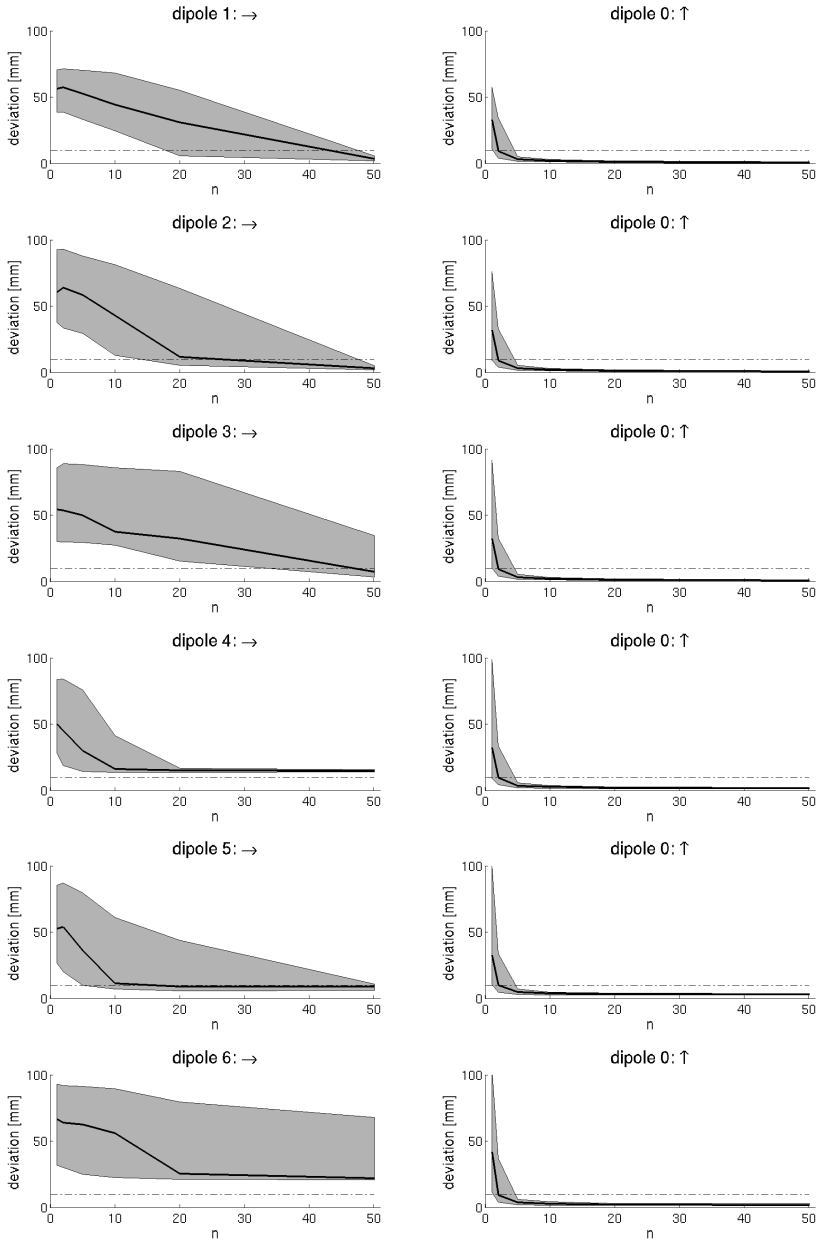

Figure B.8: Dipoles perpendicular, 5/20 nAm: distribution of deviations from target positions as a function of n.

B.2 Results of simulation 2: ratio variation

Ratio 70:30 At first, the method is run with the averaged data and both target positions. The result is shown in figure B.9.

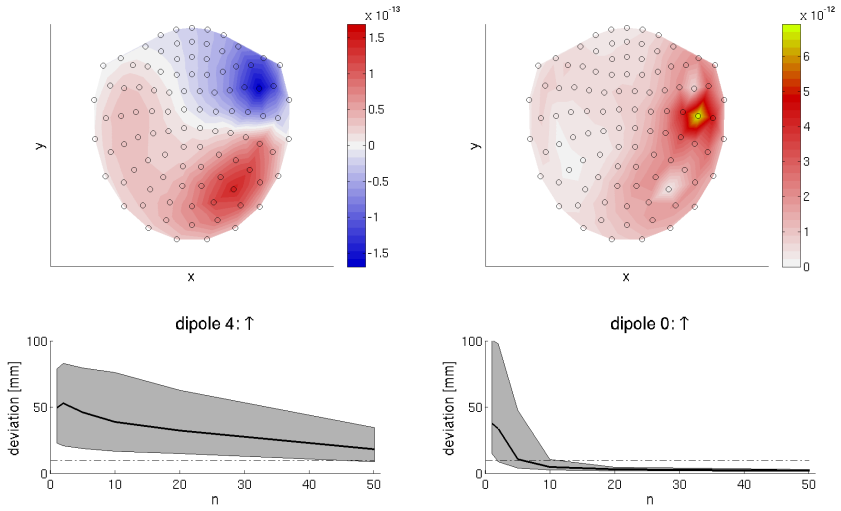

Figure B.9: Top: Magnetometer and gradiometer maps for dipoles 0 and 4 (ratio 70:30). Bottom: Distribution of deviations from target positions as a function of n.

Then only target position 0 is given. The outcome is depicted in figure B.10.

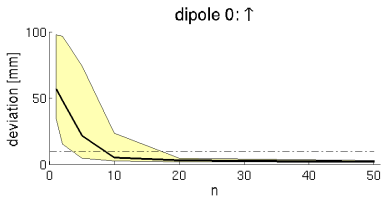

Figure B.10: Result for target position 0 with all trials.

After 30% of the trials with high deviation are marked and excluded, the procedure is repeated with $n_s = 8000$, see figure B.11.

Omitting 30% of the data has a significant influence on the localization results. Comparison of figures B.10 and B.11 demonstrates faster convergence and lower variability.

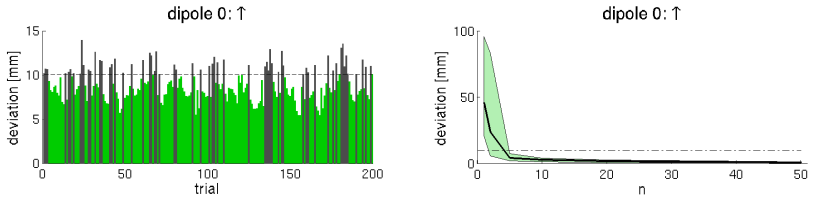

Figure B.11: Left: 30% of trials with high deviation are marked with dark gray. Hit rate is 82%. Right: Result without the marked trials.

Ratio 80:20 Figure B.12 illustrates the averaged data and the outcome of the subaveraging method with both targets.

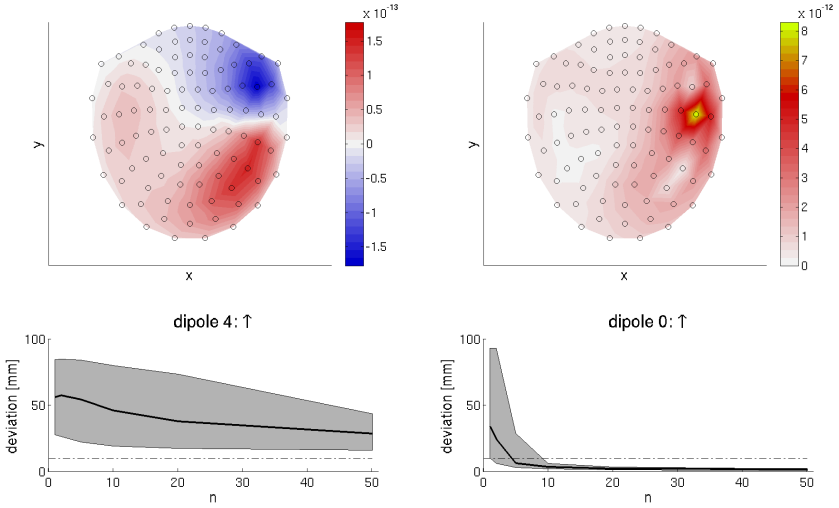

Figure B.12: Top: Magnetometer and gradiometer maps for dipoles 0 and 4 (ratio 80:20). Distribution of deviations from target positions as a function of n.

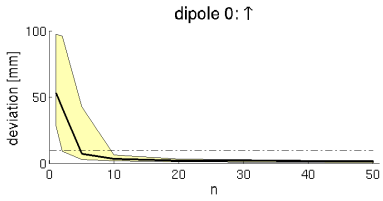

Figure B.13: Result for target position 0 with all trials.

Again, due to poor localization results, dipole 4 is not treated as a source position anymore. Only target position 0 is given. Figure B.13 depicts the

result.

The 20% of the trials with high deviation are searched and excluded. With $n_s = 8000$ the procedure is repeated. The outcome is depicted in figure B.14.

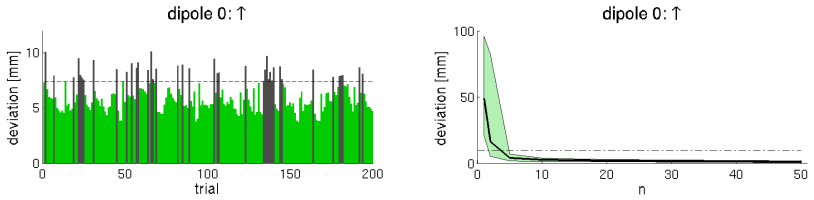

Figure B.14: Left: 20% of trials with high deviation are marked with dark gray. Hit rate is 73%. Right: Result without the marked trials.

Also 20% of the trials which do not fit into the source model have a considerable effect. Source localization improves clearly when they are removed.

Appendix C

Signal Space Separation

C.1 Solution of Laplace's equation

For the solution of Laplace's equation in spherical coordinates a separation of variables is assumed:

$$V(\mathbf{r}) \;=\; R(r)\cdot\Theta(\vartheta)\cdot\Phi(\varphi)$$

The Laplacian in spherical coordinates is given by

$$\Delta \;=\; \frac{1}{r^2}\frac{\partial}{\partial r}\left(r^2\frac{\partial}{\partial r}\right) \;+\; \frac{1}{r^2\sin\vartheta}\frac{\partial}{\partial\vartheta}\left(\sin\vartheta\frac{\partial}{\partial\vartheta}\right) + \frac{1}{r^2\sin^2\vartheta}\frac{\partial^2}{\partial\varphi^2}$$

and each differential operator only acts on its respective function, so the equation reads

$$\begin{aligned} 0 \;=\; \Delta V(\mathbf{r}) \;=\; & \underbrace{\left[\frac{\partial^2 R}{\partial r^2}+\frac{2}{r}\frac{\partial R}{\partial r}\right]\Theta\Phi}_{radial} \;+\; \underbrace{\left[\frac{\cos\vartheta}{r^2\sin\vartheta}\frac{\partial\Theta}{\partial\vartheta}+\frac{1}{r^2}\frac{\partial^2\Theta}{\partial\vartheta^2}\right]R\Phi}_{polar} \\ & + \underbrace{\left[\frac{1}{r^2\sin^2\vartheta}\frac{\partial^2\Phi}{\partial\varphi^2}\right]R\Theta}_{azimuthal} \end{aligned}$$

The radial term is connected to the Euler Differential Equation and has the solution

$$R(r) \;=\; Ar^{-l-1}+Br^{l}.$$

The polar angle term can be written as the associated Legendre Differential Equation which has the associated Legendre Polynomials as a

solution.

$$\Theta(\vartheta) \;=\; P_{lm}(\cos\vartheta)$$

Finally, the azimuthal angle term is solved by the complex exponential function.

$$\Phi(\varphi) \;=\; e^{\pm im\varphi}$$

The combination of everything gives the general solution to Laplace's equation in spherical coordinates (eq. (4.2), page 51)

$$\begin{aligned} V(\mathbf{r}) \;&=\; \sum_{l=0}^{\infty}\sum_{m=-l}^{l}\Big(\alpha_{lm}r^{-l-1} \;+\; \beta_{lm}r^{l}\Big)P_{lm}(\cos\vartheta)e^{im\varphi} \\ &=\; \sum_{l=0}^{\infty}\sum_{m=-l}^{l}\alpha_{lm}\frac{Y_{lm}(\vartheta,\varphi)}{r^{l+1}} \;+\; \sum_{l=0}^{\infty}\sum_{m=-l}^{l}\beta_{lm}r^{l}Y_{lm}(\vartheta,\varphi) \end{aligned}$$

with coefficients α_{lm} and β_{lm} and spherical harmonics $Y_{lm}(\vartheta,\varphi)$.

C.2 The gradient of spherical harmonics

For the evaluation of the gradient of spherical harmonic functions the Nabla-operator in spherical coordinates is required:

$$\nabla \;=\; \frac{\partial}{\partial r}\mathbf{e}_r \;+\; \frac{1}{r}\frac{\partial}{\partial\vartheta}\mathbf{e}_\vartheta \;+\; \frac{1}{r\sin\vartheta}\frac{\partial}{\partial\varphi}\mathbf{e}_\varphi$$

So the directional derivatives of the internal and external parts of eq. (4.2), page 51, are

$$\begin{aligned} \nabla\left[\frac{Y_{lm}(\vartheta,\varphi)}{r^{l+1}}\right] \;&=\; \begin{pmatrix} -(l+1)r^{-(l+2)}Y_{lm}(\vartheta,\varphi) \\ r^{-(l+1)}\frac{1}{r}\frac{\partial Y_{lm}(\vartheta,\varphi)}{\partial\vartheta} \\ r^{-(l+1)}\frac{1}{r\sin\vartheta}\frac{\partial Y_{lm}(\vartheta,\varphi)}{\partial\varphi} \end{pmatrix} \\ &=\; \frac{1}{r^{l+2}}\begin{pmatrix} -(l+1)Y_{lm}(\vartheta,\varphi) \\ \frac{\partial Y_{lm}(\vartheta,\varphi)}{\partial\vartheta} \\ \frac{im}{\sin\vartheta}Y_{lm}(\vartheta,\varphi) \end{pmatrix} \;=\; \frac{1}{r^{l+2}}\begin{pmatrix} \boldsymbol{\nu}_{lm}^{(r)}(\vartheta,\varphi) \\ \boldsymbol{\nu}_{lm}^{(\vartheta)}(\vartheta,\varphi) \\ \boldsymbol{\nu}_{lm}^{(\varphi)}(\vartheta,\varphi) \end{pmatrix} \end{aligned}$$

$$\nabla\left[r^l Y_{lm}(\vartheta,\varphi)\right] = \begin{pmatrix} l r^{l-1} Y_{lm}(\vartheta,\varphi) \\ r^l \frac{1}{r} \frac{\partial Y_{lm}(\vartheta,\varphi)}{\partial \vartheta} \\ r^l \frac{1}{r \sin\vartheta} \frac{\partial Y_{lm}(\vartheta,\varphi)}{\partial \varphi} \end{pmatrix}$$

$$= r^{l-1} \begin{pmatrix} l Y_{lm}(\vartheta,\varphi) \\ \frac{\partial Y_{lm}(\vartheta,\varphi)}{\partial \vartheta} \\ \frac{im}{\sin\vartheta} Y_{lm}(\vartheta,\varphi) \end{pmatrix} = r^{l-1} \begin{pmatrix} \boldsymbol{\omega}_{lm}^{(r)}(\vartheta,\varphi) \\ \boldsymbol{\omega}_{lm}^{(\vartheta)}(\vartheta,\varphi) \\ \boldsymbol{\omega}_{lm}^{(\varphi)}(\vartheta,\varphi) \end{pmatrix}$$

with the modified vector spherical harmonics $\boldsymbol{\nu}_{lm}(\vartheta,\varphi)$ and $\boldsymbol{\omega}_{lm}(\vartheta,\varphi)$. They provide the basis functions for the vector magnetic field expressed as a series expansion (eq. (4.3), page 52).

C.3 Transformation of VSH

Transformation of the modified VSH into Cartesian coordinates and projection on the sensor normals yields scalar magnetic field values. They are necessary for the calculation of basis matrices used for the series expansion representation of MEG data.

The transformation is done by use of an orthogonal rotation matrix which is obtained from the normalized Jacobian. The Jacobian is the matrix of first derivatives of a vector function of several variables. Its normalized columns are the unit vectors of the present coordinate system, spanning the vector space. With

$$\begin{aligned} x &= x(r,\vartheta,\varphi) = r\sin\vartheta\cos\varphi \\ y &= y(r,\vartheta,\varphi) = r\sin\vartheta\sin\varphi \\ z &= z(r,\vartheta,\varphi) = r\cos\vartheta \end{aligned}$$

the Jacobian reads

$$\mathbf{J} = \begin{pmatrix} \frac{\partial x}{\partial r} & \frac{\partial x}{\partial \vartheta} & \frac{\partial x}{\partial \varphi} \\ \frac{\partial y}{\partial r} & \frac{\partial y}{\partial \vartheta} & \frac{\partial y}{\partial \varphi} \\ \frac{\partial z}{\partial r} & \frac{\partial z}{\partial \vartheta} & \frac{\partial z}{\partial \varphi} \end{pmatrix} = \begin{pmatrix} \sin\vartheta\cos\varphi & r\cos\vartheta\cos\varphi & -r\sin\vartheta\sin\varphi \\ \sin\vartheta\sin\varphi & r\cos\vartheta\sin\varphi & r\sin\vartheta\cos\varphi \\ \cos\vartheta & -r\sin\vartheta & 0 \end{pmatrix}$$

Normalization of the columns gives the unit vectors

$$\mathbf{e}_r = \begin{pmatrix} \sin\vartheta\cos\varphi \\ \sin\vartheta\sin\varphi \\ \cos\vartheta \end{pmatrix} \qquad \mathbf{e}_\vartheta = \begin{pmatrix} \cos\vartheta\cos\varphi \\ \cos\vartheta\sin\varphi \\ \sin\vartheta \end{pmatrix} \qquad \mathbf{e}_\varphi = \begin{pmatrix} -\sin\varphi \\ \cos\varphi \\ 0 \end{pmatrix}$$

which make up an orthonormal basis of $\mathbb{R}^3$:

$$\mathbf{R} = \begin{pmatrix} \sin\vartheta\cos\varphi & \cos\vartheta\cos\varphi & -\sin\varphi \\ \sin\vartheta\sin\varphi & \cos\vartheta\sin\varphi & \cos\varphi \\ \cos\vartheta & \sin\vartheta & 0 \end{pmatrix}$$

This matrix is used for the transformation of a vector field $\mathbf{A}$ between Cartesian and spherical coordinate systems:

$$\begin{aligned} \big(\mathbf{A}_x, \mathbf{A}_y, \mathbf{A}_z\big)^T &= \mathbf{R} \cdot \big(\mathbf{A}_r, \mathbf{A}_\vartheta, \mathbf{A}_\varphi\big)^T \\ \big(\mathbf{A}_r, \mathbf{A}_\vartheta, \mathbf{A}_\varphi\big)^T &= \mathbf{R}^T \cdot \big(\mathbf{A}_x, \mathbf{A}_y, \mathbf{A}_z\big)^T \end{aligned}$$

where the superscript ^{T} denotes transposition.

Thus, the modified VSH $\boldsymbol{\nu}_{lm}(\vartheta,\varphi)$ and $\boldsymbol{\omega}_{lm}(\vartheta,\varphi)$ can be transformed into Cartesian coordinates and projected onto the sensor normals, which are also given in Cartesian coordinates. This completes the derivation of basis matrices $\mathbf{S}_{in}$ and $\mathbf{S}_{out}$, needed for the fundamental series expansion formula for SSS (see equations (4.4) and (4.5), page 52).

Appendix D

Software Developments

The most important implementations done for the computations in this thesis include, but are not limited to:

- Sarvas formula for calculation of the forward solution (equation (2.3), page 18)
- evaluation of vector spherical harmonics (VSH), i.e. gradients of spherical harmonics (equation (4.3), page 52)
- SSS basis vectors $\mathbf{a}_{lm}$ and $\mathbf{b}_{lm}$ (page 52)
- Taulu formula for calculation of the forward solution (equation (5.1), page 69)
- visualization of the results

Programming language was Matlab. The codes are designed for proof of concept, they are not optimized regarding computation time or required working memory.

Bibliography

Baillet S, Mosher JC, Leahy RM (2001): Electromagnetic brain mapping, *IEEE Signal Processing Magazine*, 1053-5888/01

Burghoff M, Steinhoff U, Haberkorn W, Koch H (1997): Comparability of measurement results obtained with Multi-SQUID-Systems of different sensor configurations. *IEEE Transactions on Applied Superconductivity*, 7, 2, 3465-3468

Burghoff M, Nenonen J, Trahms L, Katila T (2000): Conversion of magnetocardiographic recordings between two different multichannel SQUID devices. *IEEE Transactions on Biomedical Engineering*, 47, 7, 869-875

Gath I, Bar-On E, Lehmann D (1985): Automatic classification of visual evoked responses. *Computer Methods and Programs in Biomedicine*, 20, 17-22

Gencer NG, Tanzer IO, Özdemir MK, Acar CE, Sungur M (1998): State of the art in realistic head modeling for electro-magnetic source imaging of the human brain. *Elektrik*, 6, 3, 167-182

Geva AB, Pratt H (1994): Unsupervised clustering of evoked potentials by waveform. *Medical and Biological Engineering and Computing*, 32, 543-550

Golubic SJ, Susac A, Grilj V, Ranken D, Huonker R, Haueisen J, Supek S (2011): Size matters: MEG empirical and simulation study on source localization of the earliest visual activity in the occipital cortex. *Medical and Biological Engineering and Computing*, 49, 545-554

Greiner W (1982): Theoretische Physik Band 3: Klassische Elektrodynamik. Thun und Frankfurt am Main: Harri Deutsch, 172-179

Grunwald AG (1996): Das Verteilte-Quelle-Modell bei der Analyse von MEG-Daten - Kritische Betrachtungen zur Quellenanalyse. Dissertation, Westfälische Wilhelms-Universität Münster, Institut für Experimentelle Audiologie

Hartigan JA (1969): Using subsample values as typical values. *American Statistical Association*, 64, 1303-1317

Hauk O (2004): Keep it simple: A case for using classical minimum norm estimation in the analysis of EEG and MEG data. *Neuroimage*, 21, 1612-1621

Hämäläinen M (1992): Magnetoencephalography: A tool for functional brain imaging. *Brain Topography*, 5, 2, 95-102

Hämäläinen M, Hari R, Ilmoniemi RJ, Knuutila J, Lounasmaa OV (1993): Magnetoencephalography - theory, instrumentation, and applications to noninvasive studies of the working human brain. *Reviews of modern physics*, 65, 2, 413-497

Hämäläinen MS, Ilmoniemi R (1994): Interpreting magnetic fields of the brain: minimum norm estimates. *Medical and Biological Engineering and Computing*, 32, 35-42

Hill EL (1954): The theory of vector spherical harmonics. *American Journal of Physics*, 22, 211-214

Hülshoff T (2000): Das Gehirn: Funktionen und Funktionseinbußen. Bern: Hans Huber

Ioannides AA (2001): Real time human brain function: Observations and inferences from single trial analysis of magnetoencephalographic signals. *Clinical Electroencephalography*, 32, 98-111

Ioannides AA, Kastopoulos GK, Laskaris NA, Liu L, Shibata T, Schellens M, Poghosyan V, Khurshudyan A(2002): Timing and connectivity in the human somatosensory cortex from single trial mass electrical activity. *Human Brain Mapping*, 15, 231-246

Ioannides AA, Poghosyan V, Dammers J, Streit M (2004): Real-time neural activity and connectivity in healthy individuals and schizophrenia patients. *Neuroimage*, 23, 473-482

Ioannides AA(2006): Magnetoencephalography as a research tool in neuroscience: State of the art. *Neuroscientist*, 12, 6, 524-544

Jackson JD (1982): Klassische Elektrodynamik. Berlin, New York: Walter de Gruyter

Jänke L (2005): Methoden der Bildgebung in der Psychologie und den kognitiven Neurowissenschaften. Stuttgart: W. Kohlhammer

Jensen O, Hesse C (2010): Estimating distributed representations of evoked responses and oscillatory brain activity. In MEG: An introduction to methods. Oxford University Press, New York: Ed. by Hansen, Kringelbach, Salmelin

Knösche TR(2002): Transformation of whole-head MEG recordings between different sensor positions. *Biomedizinische Technik*, 47, 3, 59-62

Koessler L, Maillard L, Benhadid A, Vignal JP, Felblinger J, Vespignani H, Braun M (2009): Automated cortical projection of EEG sensors: Anatomical correlation via the international 10-10 system. *Neuroimage*, 46, 64-72

Laskaris NA, Ioannides AA (2002): Semantic geodesic maps: a unifying geometrical approach for studying the structure and dynamics of single trial evoked responses. *Clinical Neurophysiology*, 113, 1209-1226

Laskaris NA, Liu LC, Ioannides AA (2003): Single-trial variability in early visual neuromagnetic responses: An explorative study based on the re-

gional activation contributing to the N70m peak. *Neuroimage*, 20, 765-783

Lew S, Wolters CH, Anwander A, Makeig S, MacLeod RS (2009): Improved EEG source analysis using Low-Resolution Conductivity Estimation in a four-compartment finite element head model. *Human Brain Mapping*, 30, 2862-2878

Lew S, Wolters CH, Dierkes T, Röer C, MacLeod RS (2009a): Accuracy and run-time comparison for different potential approaches and iterative solvers in finite element method based EEG source analysis. *Applied Numerical Mathematics*, 59, 1970-1988

Liu LC, Ioannides AA, Müller-Gärtner HW (1998): Bi-Hemispheric study of single trial MEG signals of the human auditory cortex. *Electroencephalography and Clinical Neurophysiology*, 106, 64-78

Liu Z, Fukunaga M, de Zwart JA, Duyn JH (2010): Large-scale spontaneous fluctuations and correlations in brain electrical activity observed with magnetoencephalography. *Neuroimage*, 51, 102-111

Maeß B, Jacobsen T, Schröger E, Friederici AD (2007): Localizing preattentive auditory memory-based comparison: Magnetic mismatch negativity to pitch change. *Neuroimage*, 37, 561-571

Malmivuo J, Plonsey R (1995): Bioelectromagnetism - Principles and Applications of Bioelectric and Biomagnetic Fields. New York: Oxford University Press

Mattout J, Phillips C, Penny WD, Rugg MD, Friston K (2006): MEG source reconstruction under multiple constraints: An extended Bayesian framework. *Neuroimage*, 30, 753-767

Mattout J, Phillips C, Henson R, Friston K (2007): MEG source reconstruction under multiple constraints: An extended Bayesian framework. In Complex Medical Imaging, Springer Verlag, Eds: Wu JL, Ito K, Tobimatsu S, Nishida N, Fukuyama H

Mertens M, Lütkenhöner B (2000): Efficient neuromagnetic determination of landmarks in the somatosensory cortex. *Clinical Neurophysiology*, 111, 1478-1487

Numminen J, Ahlfors S, Ilmoniemi R, Montonen J, Nenonen J (1995): Transformation of multichannel magnetocardiographic signals to standard grid form. *IEEE Transactions on Biomedical Engineering*, 42, 1, 72-78

Pascual-Marqui RD (2002): Standradized low resolution brain electromagnetic tomography (sLORETA): technical details. *Methods and Findings in Experimental and Clinical Pharmacology*, 24D:5-12

Pascual-Marqui RD (2007): Discrete, 3D distributed linear imaging methods of electric neuronal activity. Part 1: Exact, zero error localization *arXiv:0710.3341 [math-ph]*, http://arxiv.org/pdf/0710.3341

Pfeifer H, Schmiedel H (1997): Grundwissen Experimentalphysik. Stuttgart und Leipzig: B. G. Teubner Verlagsgesellschaft, 195-199

Raichle ME (2008): A brief history of human brain mapping. *Trends in Neurosciences*, 32, 2, 118-126

Sarvas J (1987): Basic mathematical and electromagnetic concepts of the biomagnetic inverse problem. *Physics in Medicine and Biology*, 32, 1, 11-22

Schönherr M, Maeß B (2009): Source analysis of single trial MEG data under various noise conditions. *15th Annual Meeting of the Organization for Human Brain Mapping (OHBM)*, San Francisco, CA, USA

Schönherr M, Taulu S, Maeß B (2010): Optimizing the quality of SSS-based position transformation of MEG data. *Frontiers in Neuroscience. Conference Abstract: Biomag 2010 - 17th International Conference on Biomagnetism.*, Dubrovnik, Croatia, doi: 10.3389/conf.fnins.2010.06.00117

Smith WE, Dallas WJ, Kullmann WH, Schlitt HA (1990): Linear estimation theory applied to the reconstruction of a 3-D vector current distribution. *Applied Optics*, 29, 5, 658-667

Streit MD, Ioannides A, Sinnemann T, Wölwer W, Dammers J, Zilles K, Gaebel W (2001): Disturbed facial affect recognition in patients with schizophrenia associated with hypoactivity in distributed brain regions: A magnetoencephalographic study. *American Journal of Psychiatry*, 158, 1429-1436

Tallon-Baudry C, Bertrand O (1999): Oscillatory gamma activity in humans and its role in object representation. *Trends in Cognitive Sciences*, 3, 4, 151-162

Taulu S, Kajola M, Simola J (2003): The signal space separation method. *Abstract book of the NFSI2003 conference*, page A79, Chieti, Italy

Taulu S, Kajola M (2005): Presentation of electromagnetic multichannel data: The signal space separation method. *Journal of Applied Physics*, 97, 124905 1-10

Taulu S, Simola J, Kajola M (2005): Applications of the signal space separation method. *IEEE Transactions on Signal Processing*, 53, 9, 3359-3372

Taulu S, Simola J (2006): Spatiotemporal signal space separation method for rejecting nearby interference in MEG measurements. *Physics in Medicine and Biology*, 51, 1759-1768

Taulu S (2008): Processing of weak magnetic multichannel signals: The signal space separation method. Dissertation, Helsinki University of Technology, Helsinki, Department of Biomedical Engineering and Computational Science

Uusitalo MA, Ilmoniemi RJ (1997): Signal-space projection method for separating MEG or EEG into components. *Medical and Biological Engineering and Computing*, 35, 135-140

Vrba J, Robinson SE (2001): Signal processing in magnetoencephalography. *Methods*, 25, 249-271

Wehner DT, Hämäläinen MS, Mody M, Ahlfors SP (2008): Head movements of children in MEG: Quantification, effects on source estimation, and compensation. *Neuroimage*, 40, 541-550

Wilson HS (2004): Continuous head-localization and data correction in a whole-cortex MEG sensor. *Neurology and Clinical Neurophysiology*, 56, 1-6

Wolters CH (2003): Influence of tissue conductivity inhomogeneity and anisotropy on EEG/MEG based source localization in the human brain. Dissertation, Max Planck Institute of Cognitive Neuroscience and University of Leipzig

Wolters CH, Grasedyck L, Hackbusch W (2004): Efficient computation of lead field bases and influence matrix for the FEM-based EEG and MEG inverse problem. *Inverse Problems*, 20, 1099-1116

Acknowledgements

Writing this thesis would not have been possible without the advice and support of my supervisor Dr. Burkhard Maeß and my supervising professor Gerik Scheuermann.

I am most grateful to my colleagues at the Max Planck Institute, especially my co-workers of the MEG group in Bennewitz for their support and assistance, critical and helpful discussions, creative suggestions, as well as the friendly and warm working atmosphere. In particular, I want to name Dr. Björn Herrmann, Yvonne Wolff, Stefan Illek, Moritz Dannhauer, Mirco Fuchs, and Dr. Thomas Knösche.

I wish to thank Dr. Samu Taulu for answering all my questions about SSS.

Financially this project was enabled by Prof. Angela Friederici, Director of the Neuropsychology Department of the Max Planck Institute.

Last but not least, I owe thanks to my family for their encouragement.